Article

An IL-4 signalling axis in bone marrow drives pro-tumorigenic myelopoiesis

https://doi.org/10.1038/s41586-023-06797-9

Received: 10 March 2023

Accepted: 30 October 2023

Published online: 6 December 2023

Check for updates

Nelson M. LaMarche[1,2,3], Samarth Hegde[1,2,3,18], Matthew D. Park[1,2,3,18], Barbara B. Maier[1,2,3,17], Leanna Troncoso[1,2,3], Jessica Le Berichel[1,2,3], Pauline Hamon[1,2,3], Meriem Belabed[1,2,3], Raphaël Mattiuz[1,2,3], Clotilde Hennequin[1,2,3], Theodore Chin[1,2,3], Amanda M. Reid[1,2,3], Iván Reyes-Torres[1,2,3], Erika Nemeth[1,2,3], Ruiyuan Zhang[4], Oakley C. Olson[4], Deborah B. Doroshow[2,5,6], Nicholas C. Rohs[2,5,6], Jorge E. Gomez[2,5,6], Rajwanth Veluswamy[2,5,6], Nicole Hall[2,5,6], Nicholas Venturini[1,2,3], Florent Ginhoux[7,8,9,10], Zhaoyuan Liu[9], Mark Buckup[1,2,3], Igor Figueiredo[1,2,3], Vladimir Roudko[1,11], Kensuke Miyake[12], Hajime Karasuyama[12], Edgar Gonzalez-Kozlova[1,2,3], Sacha Gnjatic[1,2,3,5,11], Emmanuelle Passegué[4], Seunghee Kim-Schulze[1,11], Brian D. Brown[1,2,3,13], Fred R. Hirsch[2,5,6], Brian S. Kim[1,14,15,16], Thomas U. Marron[1,2,3,5,6,19] & Miriam Merad[1,2,3,5,6,11,19] ✉

Myeloid cells are known to suppress antitumour immunity[1]. However, the molecular drivers of immunosuppressive myeloid cell states are not well defined. Here we used single-cell RNA sequencing of human and mouse non-small cell lung cancer (NSCLC) lesions, and found that in both species the type 2 cytokine interleukin-4 (IL-4) was predicted to be the primary driver of the tumour-infiltrating monocyte-derived macrophage phenotype. Using a panel of conditional knockout mice, we found that only deletion of the IL-4 receptor IL-4Rα in early myeloid progenitors in bone marrow reduced tumour burden, whereas deletion of IL-4Rα in downstream mature myeloid cells had no effect. Mechanistically, IL-4 derived from bone marrow basophils and eosinophils acted on granulocyte-monocyte progenitors to transcriptionally programme the development of immunosuppressive tumour-promoting myeloid cells. Consequentially, depletion of basophils profoundly reduced tumour burden and normalized myelopoiesis. We subsequently initiated a clinical trial of the IL-4Rα blocking antibody dupilumab[2–5] given in conjunction with PD-1/PD-L1 checkpoint blockade in patients with relapsed or refractory NSCLC who had progressed on PD-1/PD-L1 blockade alone (ClinicalTrials.gov identifier NCT05013450). Dupilumab supplementation reduced circulating monocytes, expanded tumour-infiltrating CD8 T cells, and in one out of six patients, drove a near-complete clinical response two months after treatment. Our study defines a central role for IL-4 in controlling immunosuppressive myelopoiesis in cancer, identifies a novel combination therapy for immune checkpoint blockade in humans, and highlights cancer as a systemic malady that requires therapeutic strategies beyond the primary disease site.

NSCLC accounts for more than 1.6 million annual deaths worldwide[6]. A key driver of cancer progression is thought to be the tumour microenvironment (TME), which in NSCLC is dominated by macrophages that support tumour growth through diverse mechanisms[7,8]. We previously used genetic fate mapping to demonstrate that macrophages in lung tumours functionally segregate by their ontogeny: resident tissue macrophages (RTMs) arise during embryonic development and promote tissue remodelling and tumour invasiveness[9]. By contrast, monocyte-derived macrophages (mo-macs) arise from bone marrow progenitors in response to inflammatory tumour cues and promote tumour growth largely by suppressing the antitumour immune response[9,10].

We recently mapped the immune landscape of human and mouse NSCLC lesions using single-cell RNA sequencing (scRNA-seq), and found a high degree of concordance between species. These studies unveiled several insights into myeloid cell diversity within lung tumours, including an essential role for RTMs in early tumour development, the presence of several functionally distinct populations of mo-macs, and a tumour-enriched dendritic cell programme of concomitant activation and immune suppression that we termed mature dendritic cell enriched in regulatory molecules[8,9,11,12] (mregDC). The type 2 cytokine IL-4 was implicated in the control of the immunosuppressive mregDC programme, and blocking IL-4 strongly reduced lung tumour burden in mice bearing orthotopic *Kras*^{G12D}*Tp53*$^{-/-}$ (KP) lung adenocarcinoma lesions[11] (Extended Data Fig. 1a) and in the B16 melanoma pulmonary metastasis model (Extended Data Fig. 1b). Surprisingly, however, when we subsequently challenged mice lacking

A list of affiliations appears at the end of the paper.

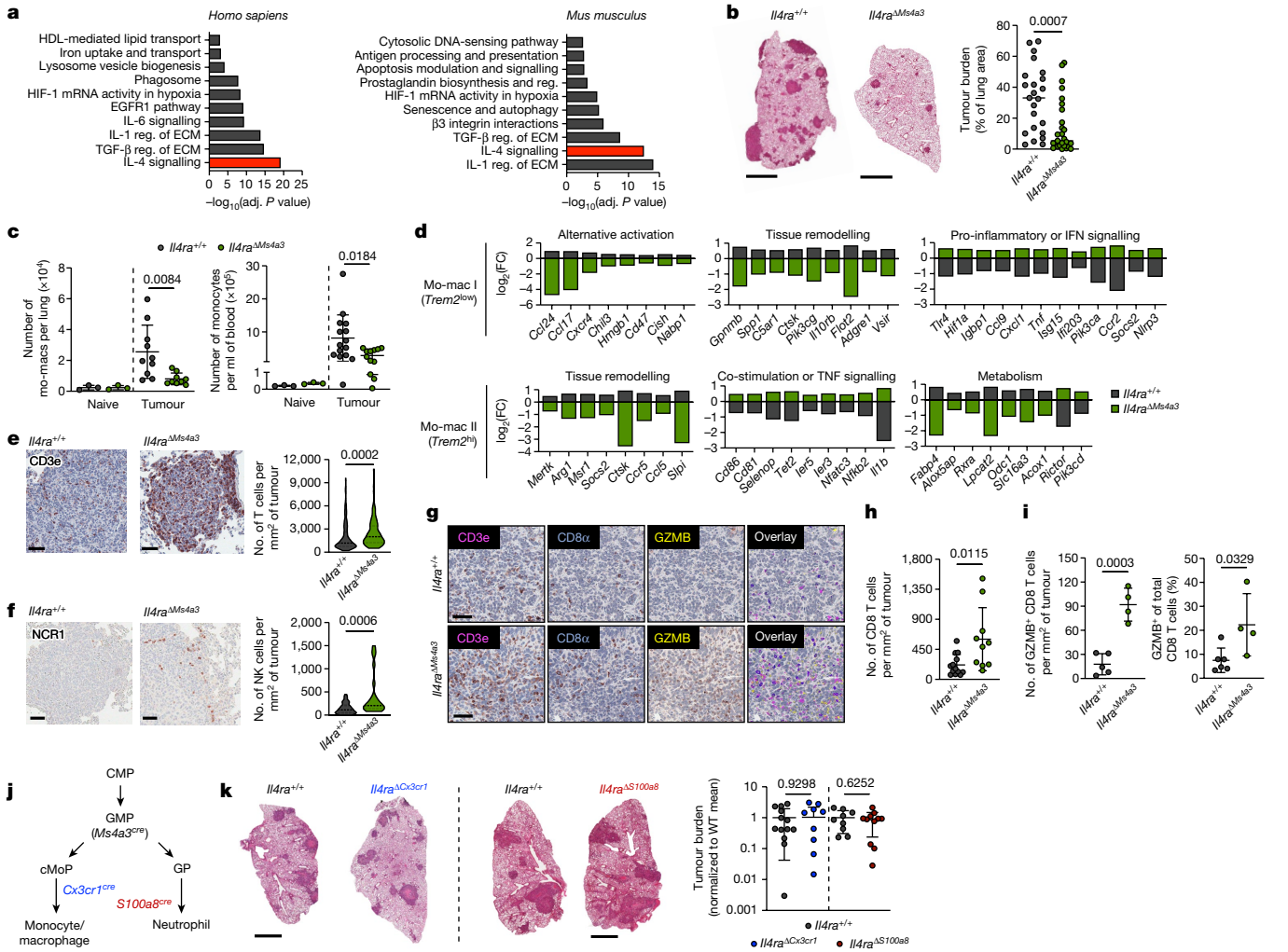

Fig. 1 | Targeted deletion of IL-4Rα in early myeloid progenitors restricts lung cancer progression. a, Top gene pathways enriched in NSCLC infiltrating mo-macs compared with normal lung RTMs from human and mouse datasets. ECM, extracellular matrix; reg., regulation. **b**, Tumour burden in KP lung tumour-bearing *Il4ra*$^{\Delta Ms4a3}$ mice ($n = 27$) and littermate controls ($n = 23$). Scale bars, 2 mm. Pooled from four independent experiments. **c**, Number of lung mo-macs and blood monocytes in naive and tumour-bearing *Il4ra*$^{\Delta Ms4a3}$ mice and littermate controls (left to right: $n = 3, 3, 10$ and 9 mice per group for mo-macs and $n = 3, 3, 15$ and 12 mice per group for monocytes). Pooled from three independent experiments. **d**, Gene expression in lung mo-mac clusters from tumour-bearing *Il4ra*$^{+/+}$ and *Il4ra*$^{\Delta Ms4a3}$ mice. $n = 3$ mice per group. One experiment. **e**, Quantification of T cells in lung tumours of *Il4ra*$^{+/+}$ ($n = 140$ tumours from 11 mice) and *Il4ra*$^{\Delta Ms4a3}$ ($n = 95$ tumours from 13 mice) mice. Pooled from three independent experiments. Scale bars, 50 µm. **f**, Quantification of natural killer (NK) cells in lung tumours of *Il4ra*$^{+/+}$ ($n = 59$ tumours from 4 mice) and *Il4ra*$^{\Delta Ms4a3}$ ($n = 22$ tumours from 7 mice) mice. Pooled from 3 out of 4 independent experiments. Scale bars, 50 µm. **g**, Immunohistochemistry co-staining of CD3e, CD8a and GZMB in lung tumours of *Il4ra*$^{+/+}$ and *Il4ra*$^{\Delta Ms4a3}$ mice. Scale bars, 50 µm. **h**, Quantification of CD8 T cells in lung tumours of *Il4ra*$^{+/+}$ ($n = 13$) and *Il4ra*$^{\Delta Ms4a3}$ ($n = 10$) mice. Pooled from three independent experiments. **i**, Average number and percentage of GZMB$^+$ CD8 T cells in lung tumours of *Il4ra*$^{+/+}$ ($n = 7$) and *Il4ra*$^{\Delta Ms4a3}$ ($n = 4$) mice. Representative of three independent experiments. **j**, Diagram of myelopoiesis showing activities of indicated Cre drivers. CMP, common myeloid progenitor; cMoP, common monocyte progenitor; GP, granulocyte progenitor. **k**, Tumour burden in KP lung tumour-bearing *Il4ra*$^{\Delta Cx3cr1}$ mice and *Il4ra*$^{\Delta S100a8}$ mice compared with littermate controls (left to right: $n = 13, 11, 9$ and 11 mice per group). Pooled from three independent experiments. Scale bars, 2 mm. WT, wild-type. Fisher's exact test (**a**); Mann–Whitney test (**b**,**e**,**f**); unpaired two-tailed Student's *t*-test (**c**,**h**,**i**,**k**). Data are median (**b**), median ± first and third quartiles (**e**,**f**), mean (**d**) or mean ± s.d. (**c**,**h**,**i**,**k**).

IL-4Rα on dendritic cells—*Il4ra*$^{\Delta DC}$, created by crossing *Zbtb46-cre*[13] mice to *Il4ra*-floxed mice—with KP cells, these mice exhibited no difference in lung tumour burden compared with wild-type littermates (Extended Data Fig. 1c). Similarly, mice specifically lacking IL-4Rα on RTMs (via *CD169-cre*[14]) or T cells (via *CD4-cre*[15]) exhibited no difference in tumour burden compared with control littermates (Extended Data Fig. 1c). As KP cells themselves did not expand in response to IL-4 treatment (Extended Data Fig. 1d), we concluded that another immune cell type must be responding to IL-4 to promote tumour development, and turned to our human and mouse NSCLC transcriptional datasets for insights.

Notably, when we performed gene set enrichment analysis (GSEA) on differentially expressed genes (DEGs) between tumour-infiltrating mo-macs and RTMs in normal lung we found that 'interleukin-4 signalling pathway' was the most highly enriched term among mo-mac-specific genes in humans and the second most highly enriched term in mice (Fig. 1a and Supplementary Table 1). We therefore crossed *Il4ra*-floxed mice to *Ms4a3-cre* mice, in which Cre is highly and transiently expressed in granulocyte-monocyte progenitors (GMPs) in bone marrow, inducing genetic deletion in all downstream immune lineages, primarily monocytes, mo-macs and neutrophils, while sparing RTMs[16] (Extended Data Fig. 1e). Upon KP tumour challenge, *Il4ra*$^{\Delta Ms4a3}$

mice exhibited an 85% reduction in tumour burden compared with wild-type littermates (Fig. 1b), pointing to a central role for IL-4 signalling within the granulocyte-monocyte lineage in tumour development. Of note, no reduction in tumour burden was seen in mice bearing an *Ms4a3-cre* allele alone without a floxed allele (Extended Data Fig. 1f), ruling out any off-target effects of Cre expression. Tumour-bearing *Il4ra*$^{\Delta Ms4a3}$ mice contained half as many lung mo-macs and circulating monocytes as littermate controls (Fig. 1c), although the numbers of circulating neutrophils (Extended Data Fig. 1g) and other lung myeloid populations (Extended Data Fig. 1h) were unchanged. Given this marked reduction in the number of mo-macs, our human transcriptional data pointing to a role for IL-4Rα signalling in the mo-mac compartment, and our detailed understanding of monocyte and macrophage molecular programmes in NSCLC, we chose to focus our studies primarily on the monocyte–mo-mac lineage.

scRNA-seq of myeloid cells in tumour-bearing lungs of both genotypes captured all the expected immune cell populations that we have described in detail elsewhere[9,11,12], including two populations of mo-macs (mo-mac I and mo-mac II) defined by low and high expression of the *Trem2* gene, respectively (Extended Data Fig. 2a). Segregating each mo-mac cluster by genotype revealed substantial differences in cells from *Il4ra*$^{\Delta Ms4a3}$ mice compared with those from wild-type littermates, including a loss of transcripts classically associated with immunosuppression (*Ccl17*, *Ccl24*, *Arg1*, *Msr1*, *Chil3* and *Hmgb1*), tissue remodelling (*Slpi*, *Gpnmb* and *Spp1*) and lipid metabolism (*Fabp4* and *Lpcat2*) and an upregulation of transcripts associated with T cell activation and costimulation (*Il1b*, *Tnf*, *Nfatc2*, *Cd86* and *Cd81*) (Fig. 1d and Extended Data Fig. 2b). Of note, many of these transcriptional changes were also present in developmentally upstream inflammatory (*Ly6c2*^{hi}) and patrolling (*Ly6c2*^{low}) monocytes (Extended Data Fig. 2b).

In line with a central role for mo-macs and monocytes in immune suppression in NSCLC, immunohistochemistry revealed that lung tumours in *Il4ra*$^{\Delta Ms4a3}$ mice contained twice as many T cells (CD3e$^+$; Fig. 1e) and natural killer cells (NCR1$^+$; Fig. 1f) as wild-type littermate controls. This was notable, as it has been demonstrated that these two lymphocyte populations are essential for tumoricidal immune control of KP lesions[11,12,17,18]. Using multiplexed immunohistochemistry (Fig. 1g), we found that both cytotoxic CD8 T cells (Fig. 1h) and helper CD4 T cells (Extended Data Fig. 2c) were similarly enriched in *Il4ra*$^{\Delta Ms4a3}$ tumours, with CD8 T cells notably expanding to fourfold their number in wild-type mice. Concordantly, multiplexed immunohistochemistry of CD3e$^+$CD8a$^+$ CD8 T cells revealed an increased absolute number and percentage of cells expressing the cytotoxic effector molecule GZMB in tumours of *Il4ra*$^{\Delta Ms4a3}$ mice (Fig. 1i). scRNA-seq of total T cells from lung tumours of each genotype followed by fine clustering of CD8 T cells identified clusters in all states of activation (Extended Data Fig. 2d). Notably, *Il4ra*$^{\Delta Ms4a3}$ lungs contained a reduced proportion of exhausted CD8 T cells[19,20] (expressing the classical exhaustion genes *Tox*, *Pdcd1*, *Tigit* and *Lag3*) and an increased proportion of effector CD8 T cells[21–23] (expressing *Gzmb*, *Ikzf2* and *Malt1*) (Extended Data Fig. 2e). Thus, loss of *Il4ra* in all GMP-derived lineages enhanced monocyte and mo-mac immunogenicity and reprogrammed the lung TME towards an inflamed antitumour state.

As *Ms4a3-cre* targets both the monocyte and neutrophil lineages, we next crossed *Il4ra*-floxed mice to *Cx3cr1-cre*[24] or *S100a8-cre*[25] drivers, which are expressed in more mature myeloid cells downstream of the GMP and are strongly biased towards the monocyte and neutrophil lineages, respectively[26] (Fig. 1j). Of note, *S100a8-cre* deletion was specific to the granulocyte lineage, despite the fact that *S100a8* is expressed at low levels in other myeloid cells in settings of inflammation (Extended Data Fig. 3). Unexpectedly, neither *Il4ra*$^{\Delta Cx3cr1}$ mice nor *Il4ra*$^{\Delta S100a8}$ mice exhibited a reduction in lung tumour burden when challenged with KP cells, despite efficient deletion of IL-4Rα in the targeted cell populations (Fig. 1k). Therefore, although deletion of IL-4Rα in early myeloid progenitors in bone marrow drove substantial remodelling of the lung TME and reduction in lung tumour burden, deletion in mature mo-macs and neutrophils had no effect.

On the basis of these data, we hypothesized that the relevant IL-4 signalling instructing the immunosuppressive mo-mac state in NSCLC occurred at an upstream stage in the mo-mac developmental pathway, before the cells' arrival at the tumour site. Indeed, we observed little evidence for a strongly T helper 2 (T_H2)-biased TME in human and mouse lung tumours. Upon querying The Cancer Genome Atlas (TCGA) NSCLC database, we observed little expression of *IL4* in tumour tissues or adjacent normal lung (Extended Data Fig. 4a). Consistent with this, *IL4* expression was nearly undetectable in all T cell clusters in our human NSCLC scRNA-seq dataset (Extended Data Fig. 4b). Our analysis of mouse tumour-bearing lungs supported this conclusion; we observed essentially no IL-4-producing CD4 T cells in tumour-bearing mice, either by pharmacological stimulation with phorbol myristate acetate and ionomycin or by using *IL4*-eGFP (4get) mice, in which a GFP reporter identifies all *IL4*-producing cells[27], although total eGFP positivity increased marginally to 0.02% of live cells (Extended Data Fig. 4c). Furthermore, KP tumour cells did not produce IL-4 at the transcript[9] or protein level (Extended Data Fig. 4d).

Consistent with our hypothesis, pathway analysis of DEGs between *Il4ra*$^{+/+}$ and *Il4ra*$^{\Delta Ms4a3}$ tumour-infiltrating monocytes revealed several pathway hits associated with myeloid development and differentiation (Extended Data Fig. 5a). Indeed, *Il4ra*$^{\Delta Ms4a3}$ monocytes expressed much higher levels of genes associated with monocyte maturation, including the receptor-encoding genes *Csf1r* and *Csf2rb* and the transcription factor genes *Nr4a1* and *Nr4a2*[28] (Fig. 2a). They concomitantly expressed lower levels of *Ly6a* (which encodes SCA-1, a receptor that is highly expressed on early haematopoietic progenitors), *Bach2* and *S100a9*, which are all associated with early stages of myeloid development[29,30] (Fig. 2a). This was notable, as immature myeloid cells induced by emergency myelopoiesis in bone marrow have been widely reported in tumour-bearing mice and human cancer patients[31].

We therefore examined myeloid progenitor populations in the bone marrow of *Il4ra*$^{+/+}$ and *Il4ra*$^{\Delta Ms4a3}$ mice. We first confirmed by flow cytometry that tumour cells had not metastasized to the bone marrow in our model (Extended Data Fig. 5b). We used a general, unifying definition for GMPs that have passed the common myeloid progenitor stage based on surface markers[16,32] (lineage$^-$Sca-1$^-$CD135$^-$KIT$^+$CD34$^+$CD16/CD32^{hi}). We observed no difference in GMP number between genotypes in naive mice (Fig. 2b). However, whereas *Il4ra*$^{+/+}$ tumour-bearing mice exhibited twofold expansion of GMPs in accordance with enhanced myelopoiesis, this expansion was completely abrogated in *Il4ra*$^{\Delta Ms4a3}$ mice (Fig. 2b). GMP expansion was also abrogated by treating wild-type tumour-bearing mice with IL-4 blocking antibodies (Extended Data Fig. 5c). The surface markers LY6C and CD115 have been proposed to segregate the bulk GMP population into more discrete populations with biased developmental trajectories, such as LY6C$^-$ GMPs (LY6C$^-$CD115$^-$) with similar monocyte and granulocyte developmental potential, granulocyte progenitors (GPs; LY6C$^+$CD115$^-$), which are more biased towards the granulocyte lineage, and common monocyte progenitors (cMoPs; LY6C$^+$CD115$^+$) biased towards monocyte development[16,33,34]. Gating on each of these subpopulations individually revealed that expansion of the multipotent LY6C$^-$ GMP was most strongly abrogated in *Il4ra*$^{\Delta Ms4a3}$ tumour-bearing mice (Extended Data Fig. 5d). Next, we tested whether myeloid progenitors in bone marrow of tumour-bearing mice engage signalling through IL-4Rα. We used flow cytometric staining for phosphorylated STAT6 (pSTAT6), a transcription factor that is phosphorylated at Y641 immediately upon binding of the IL-4Rα to IL-4 or IL-13[35]. Whereas all GMP subpopulations expressed low baseline pSTAT6, staining increased threefold upon tumour challenge (Fig. 2c), demonstrating that the bone marrow is a relevant site of myeloid IL-4Rα signalling in NSCLC.

Next, we tested whether IL-4Rα signalling in bone marrow controls monocyte differentiation and if so, whether it imprints specific

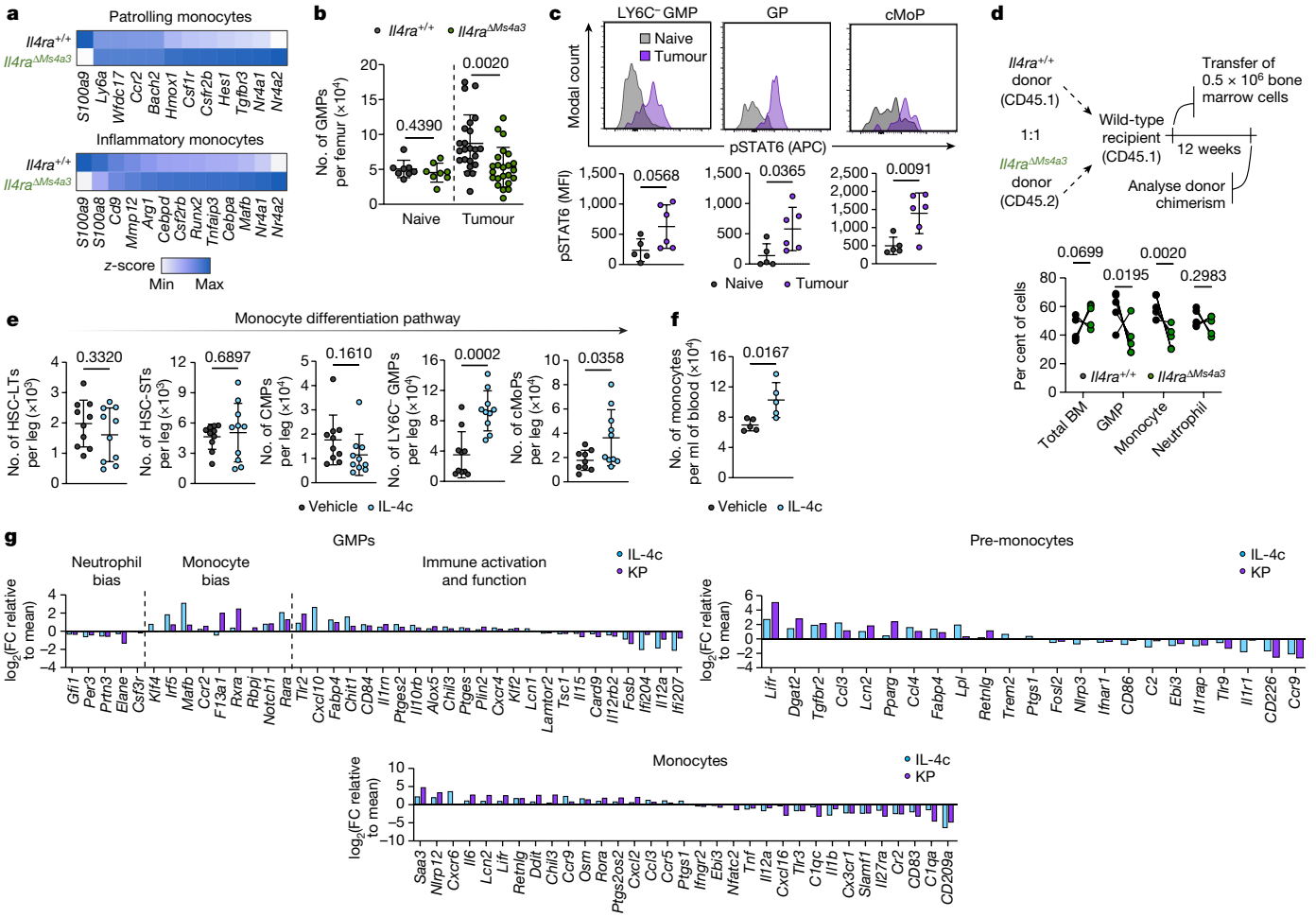

Fig. 2 | Local IL-4 signalling in bone marrow fuels immunosuppressive myelopoiesis. a, Relative expression of statistically significant maturation-associated genes in lung monocyte populations from *Il4ra*$^{+/+}$ and *Il4ra*$^{\Delta Ms4a3}$ tumour-bearing mice ($n = 3$ mice per group). **b**, Number of bulk GMPs per femur in naive and tumour-bearing *Il4ra*$^{+/+}$ and *Il4ra*$^{\Delta Ms4a3}$ mice (left to right: $n = 8, 8, 23$ and 23 mice per group). Pooled from three independent experiments. **c**, pSTAT6 staining in indicated bone marrow myeloid progenitors in naive ($n = 5$) and KP tumour-bearing ($n = 6$) mice. Representative of two independent experiments. MFI, mean fluorescence intensity. **d**, Proportion of wild-type (CD45.1) and *Il4ra*$^{\Delta Ms4a3}$ (CD45.2) cells in indicated cell populations in mice reconstituted with 1:1 (wild-type:*Il4ra*$^{\Delta Ms4a3}$) bone marrow (BM) cells 12 weeks post-transplant ($n = 5$ mice per group). One experiment. **e**, Number of indicated haematopoietic progenitor populations in bone marrow of vehicle and IL-4c injected mice ($n = 10$ mice per group). Pooled from two independent experiments. HSC-LT, long-term haematopoietic stem cell (HSC). HSC-ST, short-term HSC. **f**, Number of monocytes per millilitre of blood in vehicle and IL-4c injected mice ($n = 5$ mice per group). Representative of two independent experiments. **g**, Curated gene lists showing indicated genes in GMP, pre-monocyte and monocyte clusters of IL-4c and KP-treated mice relative to naive controls. FC, fold change. Unpaired two-tailed Student's *t*-test. Data are mean ± s.d.

molecular programmes on downstream macrophages. We first performed competitive bone marrow chimeras, in which lethally irradiated mice were reconstituted with a 1:1 mixture of wild-type (CD45.1) and *Il4ra*$^{\Delta Ms4a3}$ (CD45.2) bone marrow cells. Of note, whereas total bone marrow cells engrafted equally between the two genotypes, we found that *Il4ra*$^{\Delta Ms4a3}$ GMPs and downstream blood monocytes expanded significantly less than their wild-type counterparts within the same animal (Fig. 2d), pointing to a competitive advantage for IL-4Rα signalling in monopoiesis at steady state. Similarly, *Il4ra*$^{\Delta Ms4a3}$ haematopoietic progenitors were limited in their ability to differentiate towards the granulo-macrophage lineage (Extended Data Fig. 5e). To further establish the role of IL-4 signalling on bone marrow myelopoiesis we treated wild-type mice with IL-4 complexes (IL-4c) (in which IL-4 is stabilized by IL-4 antibodies to extend its in vivo half-life[36]) or vehicle control, and quantified bone marrow intermediates in the monocytic developmental pathway from the earliest haematopoietic stem cells (HSCs) to blood monocytes. IL-4c treatment had no effect on the earliest HSCs, but induced a sharp and profound expansion of GMPs and all downstream populations, with LY6C^{-} GMPs exhibiting a threefold expansion over four days (Fig. 2e,f and Extended Data Fig. 5f,g). Of note, injection of the relevant isotype IgG1κ alone did not induce expansion of progenitor populations (Extended Data Fig. 5h). Additionally, GMPs from *Il4ra*$^{\Delta Ms4a3}$ mice did not expand upon IL-4c injection (Extended Data Fig. 5i).

To determine whether early IL-4 signalling at the myeloid progenitor stage affects the phenotype of mature macrophages, we first turned to a reductionist in vitro system. Alternatively activated M2 macrophages are commonly differentiated in vitro by culturing bone marrow in M-CSF to generate M0 bone marrow-derived macrophages (BMDMs) followed by polarization with IL-4[12]. We modified this protocol to reflect what our data suggests occurs in NSCLC by instead treating bone marrow with IL-4 for the first two days of culture—before macrophage differentiation—then removing IL-4 and culturing nonadherent cells in M-CSF for an additional five days to generate IL-4-primed BMDMs, and compared them with conventional M0 and M2 BMDMs. Notably, priming myeloid progenitors with IL-4 was sufficient to fully induce an M2 phenotype in downstream BMDMs—including an upregulation of the canonical M2 markers ARG-1, CD206 and PD-L1 and a downregulation

of the T cell activating molecules IL-12p40 and CD86 (Extended Data Fig. 5j).

To extend these observations to a relevant in vivo setting, we performed scRNA-seq of bone marrow myeloid cells and progenitors from naive, IL-4c-treated, and KP lung tumour-bearing mice. In addition to bona fide monocytes and neutrophils, clustering resolved several myeloid progenitor populations. Using several well-referenced bone marrow transcriptional datasets[16,37–39], we annotated these clusters as GMPs (corresponding with LY6C$^-$ GMPs by flow cytometry and expressing *Mpo*, *Elane*, *Prtn3* and the GMP-defining gene *Ms4a3*) as well as pre-monocytes (corresponding with cMoPs by flow cytometry and expressing GMP genes as well as high levels of *Ccr2*, *F13a1*, *Klf4*, *Irf5*, *Irf8* and *Vcan*) and pro-neutrophils (corresponding with GPs by flow cytometry and expressing high levels of *Ly6g*, *S100a8*, *S100a9*, *Mmp8*, *Ccl6*, *Cebpe*, *Gfi1* and *Per3*), which had begun to differentiate away from the GMP state (Extended Data Fig. 5k). Within each population along the monocyte differentiation pathway (GMPs, pre-monocytes and monocytes), we analysed DEGs in cells from IL-4c-treated and KP-bearing mice compared with those from naive controls. IL-4c and KP challenge each induced major transcriptional alterations in these compartments, and there was a remarkable degree of overlap, with nearly 40% of all upregulated and downregulated genes being shared between the two conditions (Extended Data Fig. 5l).

We next examined condition-specific DEGs within each of these three populations, focusing on genes that exhibited similar behaviours in IL-4c and KP-treated groups compared with naive control (Fig. 2g and Supplementary Table 2). Within the GMP compartment, both IL-4c and KP challenge induced a clear bias towards monocyte differentiation, with a downregulation of granulocytic genes (*Elane*, *Gfi1* and *Per3*) and an upregulation of monocyte-specifying genes (*Ccr2*, *Mafb* and *Rara*). These two treatments also induced several immunosuppressive gene programmes in GMPs that are frequently associated with tumour-promoting myeloid cells, with an upregulation of genes promoting T cell suppression and lipid metabolism (*Ccl3*, *Chit1*, *Il10rb*, *Ptges*, *Ptges2* and *Alox5*) and a downregulation of immunostimulatory genes (*Il12a*, *Il12rb2*, *Card9* and *Il15*). This archetype was maintained and expanded in pre-monocytes and downstream monocytes, which continued to express higher levels M2 macrophage associated genes such as *Retnlg*, *Ccl3*, *Ccl4* and *Dgat2*, and downregulated additional genes that promote cytotoxic immunity such as *Nlrp3*, *CD86*, *Il1r1*, *CD226* and *Tnf*.

Thus, several transcriptional changes that are essential for promoting an immunosuppressive TME are induced in bone marrow myeloid progenitors before their arrival at the tumour site, and these changes can be recapitulated by exposing bone marrow to IL-4 in vivo. This, combined with our findings that only deletion of *Il4ra* in early myeloid progenitors reduces lung tumour burden (Fig. 1) and that myeloid progenitors engage IL-4Rα signalling in tumour-bearing mice (Fig. 2c), points to a central role for a bone marrow-intrinsic IL-4Rα signalling pathway in NSCLC development.

Next, we explored the cell types that produce IL-4 to control immunosuppressive myelopoiesis in NSCLC. Consistent with our findings that IL-4 was not highly produced in the lung TME and the fact that IL-4 has an extremely short half-life, we could not detect any IL-4 protein in lung homogenate or in circulating blood of tumour-bearing mice (limit of detection 1 pg ml^{-1} (data not shown)). Therefore, we hypothesized that local cells within bone marrow were the relevant sources of IL-4. Using 4get mice, we found that almost all *IL4*-eGFP produced in bone marrow of tumour-bearing mice was derived from eosinophils and basophils, which collectively constituted roughly 5% of cells in bone marrow (Fig. 3a and Extended Data Fig. 6a,b). These cells—often called type 2 granulocytes because of their ability to produce several type 2 effector cytokines—are typically rare to absent in peripheral tissues at steady state, but accumulate rapidly in response to T_H2-driven inflammation[31]. Although bone marrow eosinophils and basophils did not increase in number in tumour-bearing mice (Extended Data Fig. 6c), they markedly upregulated their expression of *IL4*-eGFP compared with naive controls (Fig. 3b). We therefore hypothesized that bone marrow type 2 granulocytes are the key cell types driving IL-4 dependent aberrant myelopoiesis in NSCLC.

We sought to test this hypothesis by deleting an IL-4 source specifically within the bone marrow. Using intravenous (IV) CD45 labelling, which segregates immune cells that have entered the lung parenchyma (CD45-IV$^-$) from extra-tissular cells circulating through the blood[40] (CD45-IV$^+$), we found that eosinophils rapidly entered the lung parenchyma upon tumour challenge (Fig. 3c and Extended Data Fig. 6d); however, 100% of basophils remained in the circulation (CD45-IV$^+$) in both naive and tumour-bearing mice and did not migrate into lung tumours (Fig. 3c and Extended Data Fig. 6d). We confirmed this with immunohistochemistry staining for the basophil-specific marker mast cell protease 8[41] (MCP-8), and observed no basophil infiltration in lung tumours across 12 mice (Fig. 3d). By contrast, basophils were enriched in bone marrow and made intimate contact with KIT$^+$ haematopoietic progenitors in tumour-bearing mice, as measured by immunofluorescence microscopy (Extended Data Fig. 6e). Thus, we reasoned that specific depletion of basophils would eliminate a major source of IL-4 in bone marrow while leaving any IL-4 production in the lung tumour unaltered.

We thus implanted mice with KP tumours and used two orthogonal antibody-mediated strategies to deplete basophils—anti-FCER1A, which deplete basophils, but also mast cells and a small population of dendritic cells[42]; and anti-CD200R3, which induces highly specific depletion of the basophil lineage[43]. We confirmed efficient depletion of peripheral and bone marrow basophils with each of these antibodies (Extended Data Fig. 6f). In both cases, basophil depletion profoundly reduced tumour burden compared with mice receiving control isotype antibodies (Fig. 3d,e). Consistent with our model of basophil IL-4 being a central driver of myelopoiesis in cancer, basophil-depleted mice exhibited a strong reduction in bone marrow GMPs, which translated into reduced lung monocytes and lung mo-macs (Fig. 3f). Thus, basophils are a dominant *IL4* source in bone marrow that are not present in lung tumours, and their depletion abrogates immunosuppressive myelopoiesis and reduces tumour burden.

We next aimed to identify the factors that drive bone marrow basophils to produce IL-4 in tumour-bearing mice. Solid tumours are known to influence haematopoiesis through soluble factors produced both by the tumour cells themselves and by stromal components[44,45]. In line with this, culture of 4get bone marrow basophils with KP cell-conditioned medium drove marked upregulation of *IL4*-eGFP (Fig. 3i). We next performed a Luminex multiplex ELISA to survey proteins in lung homogenate of naive and KP tumour-bearing wild-type mice. Notably, eight proteins reported to induce IL-4 production in basophils[46] were upregulated in the lungs of tumour-bearing mice: IL-18, VEGF-A, IL-6, IL-1α, IL-7, CCL3, IL-15 and CSF2 (Fig. 3j). Six of these proteins were also upregulated in the serum of treatment-naive patients with NSCLC compared with healthy controls, as measured by the Olink assay inflammation panel, and three—IL-6, VEGF-A and IL-18—were statistically significant (Fig. 3k and Supplementary Tables 3 and 4). We then directly tested the ability of each of these eight cytokines to induce *IL4* in bone marrow basophils in individual culture. Many of these cytokines induced modest upregulation of *IL4*-eGFP in 4get basophils when cultured alone; however, there was clear synergy when all cytokines were combined together, with basophils exhibiting a twofold upregulation of GFP mean fluorescence intensity when cultured with the combination cocktail of eight cytokines (Fig. 3l). Therefore, multiple cytokines produced in human and mouse NSCLC work collaboratively to induce IL-4 production within the bone marrow compartment. Collectively, these data define a model in which bone marrow type 2 granulocytes sense distal cues produced by NSCLC tumours and subsequently direct the development of immunosuppressive myeloid cells through the production of IL-4.

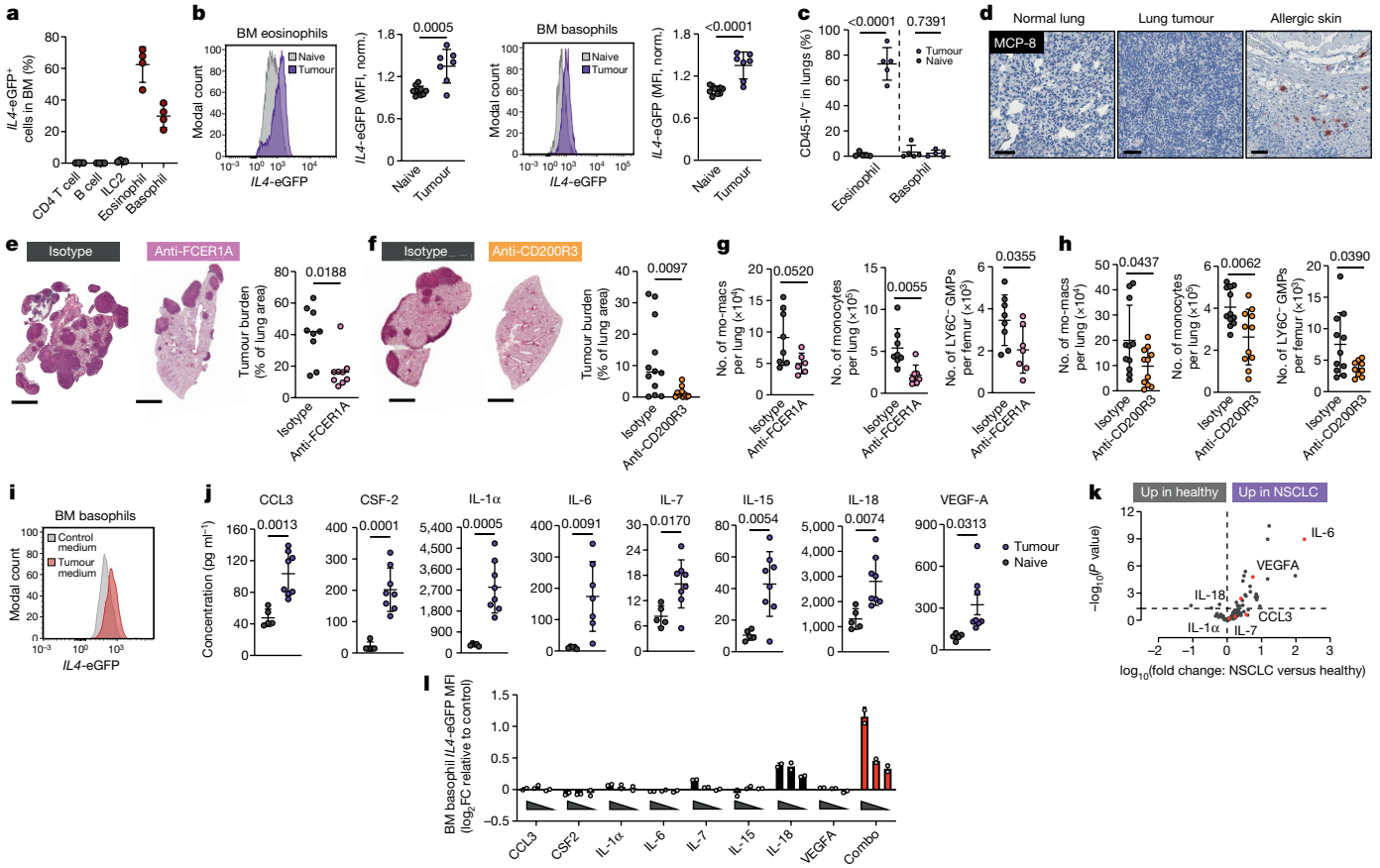

Fig. 3 | Type 2 granulocytes in bone marrow upregulate IL-4 and control myeloid output in response to distal tumour cues. a, Proportion of indicated cell type among *IL4*-eGFP$^+$ cells in bone marrow of tumour-bearing mice ($n = 4$ mice). Representative of two independent experiments. **b**, *IL4*-eGFP expression in bone marrow eosinophils and basophils from naive ($n = 10$) and tumour-bearing ($n = 7$) mice. Pooled from two independent experiments. Norm., normalized. **c**, Percentage of lung parenchymal eosinophils and basophils in naive and tumour-bearing mice ($n = 5$ mice per group). Representative of two independent experiments. **d**, Immunohistochemistry for MCP-8 in indicated tissues. Representative of 12 mice. Scale bars, 50 µm. **e**, Tumour burden in KP-bearing mice treated with anti-FCER1A or isotype antibodies ($n = 9$ mice per group). Pooled from two independent experiments. Scale bars, 2 mm. **f**, Tumour burden in KP-bearing mice treated with anti-CD200R3 ($n = 11$) or isotype ($n = 12$) antibodies. Pooled from two independent experiments. Scale bars, 2 mm. **g**, Immune cell populations in tumour-bearing mice treated with anti-FCER1A or isotype antibodies. $n = 8$ isotype and $n = 7$ anti-FCER1A-treated mice for mo-macs. $n = 8$ isotype and $n = 7$ anti-FCER1A-treated mice for monocytes and LY6C$^-$ GMPs. Representative of two independent experiments. **h**, Immune cell populations in tumour-bearing mice treated with anti-CD200R3 or isotype antibodies. $n = 11$ mice per group for mo-macs. $n = 12$ isotype and 11 anti-CD200R3-treated mice for monocytes. $n = 11$ isotype and 9 anti-CD200R3-treated mice for LY6C$^-$ GMPs. Pooled from two independent experiments. **i**, *IL4*-eGFP expression in bone marrow basophils cultured in control or tumour-conditioned medium. Representative of two independent experiments. **j**, Expression of proteins in lung homogenate of naive ($n = 5$) and tumour-bearing ($n = 8$) mice. Pooled from two independent experiments. **k**, Inflammatory proteins upregulated in plasma of treatment-naive patients with NSCLC ($n = 29$) compared with healthy controls ($n = 21$). Analytes also upregulated in **j** are indicated in red. One experiment. **l**, Expression of *IL4*-eGFP in bone marrow basophils cultured with indicated cytokines normalized to control medium. Two technical replicates per condition, representative of two independent experiments. Combo, combined cytokine cocktail. Unpaired two-tailed Student's *t*-test (**b**,**c**,**g**,**h**,**j**,**k**) or Mann–Whitney Test (**e**,**f**). Data are mean ± s.d. (**a**–**c**,**g**,**h**,**j**,**k**) or median (**e**,**f**).

Finally, we tested whether this newfound insight could be harnessed for the treatment of human lung cancer. Immune checkpoint blockade directed against the PD-1/PD-L1 pathway has revolutionized treatment for early and late-stage NSCLC; however, fewer than half of patients respond, necessitating the development of novel therapeutic approaches to improve outcomes[47–49]. We found that in mice bearing orthotopic HKP1 tumours, a variant of KP tumours that is more immunogenic and is partially responsive to checkpoint blockade[50], anti-IL-4 treatment enhanced the response to anti-PD-L1 immunotherapy, suggesting synergistic effects (Fig. 4a). On the basis of these preclinical data, we designed and opened a phase Ib trial in which patients with relapsed/refractory NSCLC who had progressed on PD-1/PD-L1 blockade continue PD-1/PD-L1 blocking antibody treatment while adding IL-4Rα blockade with dupilumab (Regeneron/Sanofi) in an attempt to induce or rescue an antitumour immune response (ClinicalTrials.gov Identifier NCT05013450). Dupilumab is a fully humanized monoclonal antibody to IL-4Rα, which disrupts signalling through receptors for both IL-4 and IL-13, and is clinically active and US Food and Drug Administration-approved for numerous atopic conditions[2–5]. The use of dupilumab has yet to be explored specifically in cancer.

We recruited six patients with NSCLC lacking targetable driver mutations who had radiographic evidence of progressive disease while on treatment with PD-1/PD-L1 blocking antibodies as part of standard of care (SOC) therapy (Supplementary Table 5). PD-1/PD-L1 blockade was continued per SOC, while patients received dupilumab subcutaneously every 3 weeks for 3 doses, with 600 mg loading dose on day 1 and 300 mg for subsequent maintenance doses, administered concomitantly with continuing PD-1/PD-L1 blocking antibodies (Fig. 4b). We observed no dose-limiting toxicities or treatment-related adverse

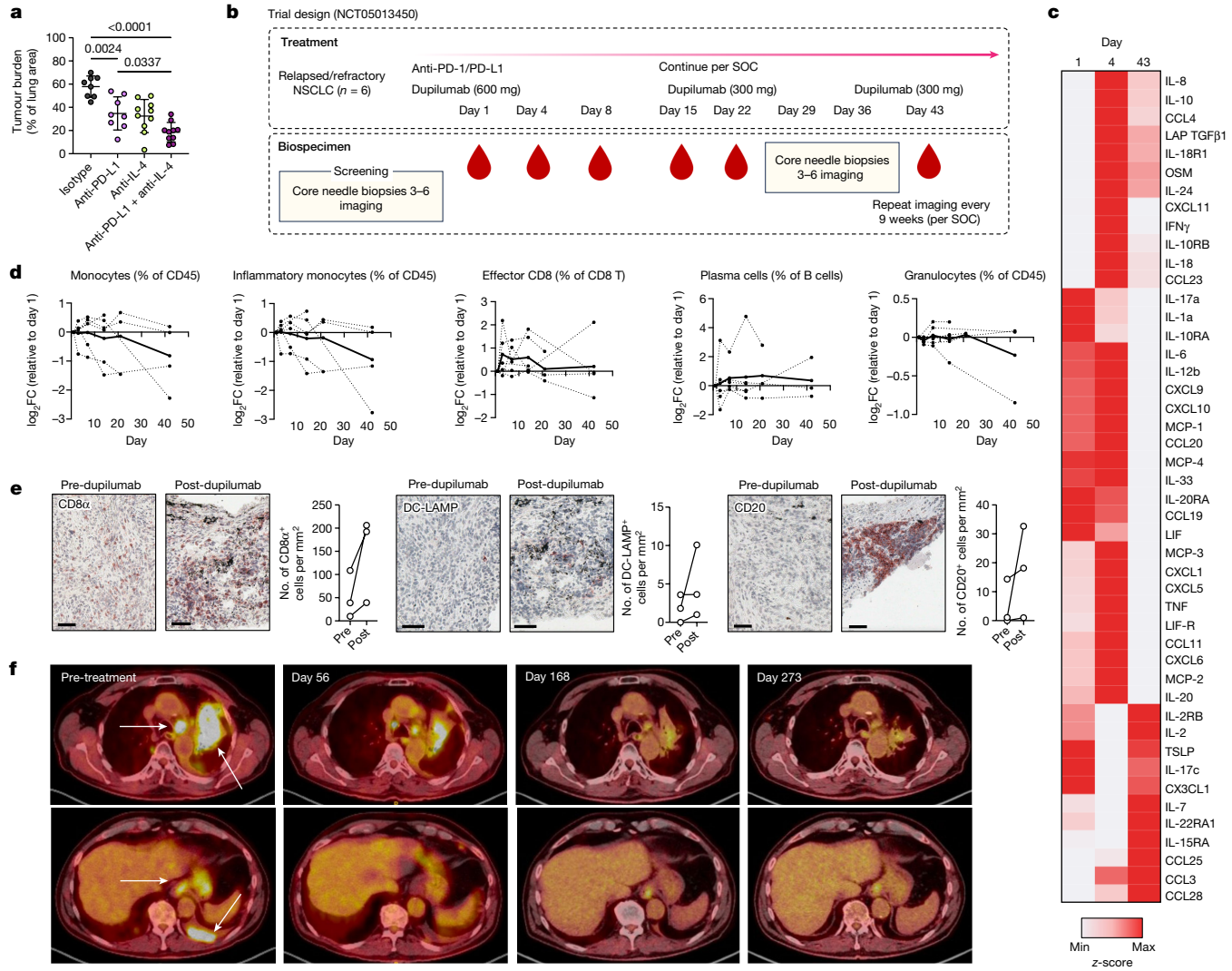

Fig. 4 | IL-4Rα blockade enhances response to immunotherapy in human NSCLC. a, Lung tumour burden in mice transplanted with HKP1 cells and treated with anti-PD-L1, anti-IL-4, or a combination of both (left to right: $n = 8, 8, 10$ and 10 mice per group). Pooled from two independent experiments. One-way ANOVA with post hoc Tukey's multiple comparison test. **b**, Clinical trial design. Pre-treatment blood is drawn on day 1. **c**, Averaged heat map of Olink inflammation panel analytes in patient plasma at indicated timepoints after dupilumab treatment. **d**, Levels of indicated immune cells in patient whole blood at indicated timepoints after dupilumab treatment as assessed by CyTOF, normalized to day 1 (pre-dupilumab treatment). Dotted lines represent individual patients; the solid line represents mean of all patients. **e**, Number of CD8, DC-LAMP and CD20-positive cells in tumour biopsies of relapsed or refractory patients with NSCLC before and 36 days after initiation of dupilumab treatment, as measured by immunohistochemistry ($n = 3$ patients). Scale bars, 50 µm. **f**, Chest computed tomography scans of a dupilumab responder before treatment and 56, 168 and 273 days after treatment. **b**–**f**, Representative of one clinical cohort.

events. Notably, we found that dupilumab co-administration drove a rapid (day 4) upregulation of proinflammatory cytokines that are known to promote antitumour immune responses, including central drivers of the T helper 1 (T_H1) immune axis (IFNγ and IL-12), and the T cell-recruiting chemokines CCL19, CXCL9, CXCL10 (Fig. 4c). Long-term (day 43), T effector cell-expanding cytokines were upregulated, including IL-2, IL-7, CCL25 and IL-15RA (Fig. 4c and Supplementary Table 6). Cytometry by time of flight (CyTOF) on whole blood revealed a steady reduction of inflammatory ($CD14^+$) monocytes over time in several patients but a minimal effect on circulating granulocytes (Fig. 4d), mirroring our results in tumour-bearing *Il4ra*$^{\Delta Ms4a3}$ mice. Additionally, dupilumab induced an expansion of circulating effector CD8 T cells and antibody-producing plasma cells, both of which are essential for the response to PD-1/PD-L1 blockade[51,52] (Fig. 4d). Immunohistochemical analysis of paired tumour biopsies from 3 patients obtained before and 36 days after dupilumab initiation revealed a concomitant remodelling of the TME. Dupilumab induced an expansion of CD8 T cells ($CD8\alpha^+$), activated dendritic cells ($DC\text{-}LAMP^+$) and B cells ($CD20^+$) in all patients who were analysed (Fig. 4e), indicating an enhanced capacity for T cell priming and cytotoxic immune function in response to PD-1/PD-L1 blockade.

Notably, one of these six patients experienced a partial clinical response on imaging, per RECIST (response evaluation criteria in solid tumours) criteria[53]. Per the protocol, this patient continued to receive maintenance checkpoint blockade concurrently with the dupilumab, and after the three doses of dupilumab, continued maintenance pembrolizumab alone after the first imaging; two subsequent radiographic evaluations demonstrated deepening of the radiographic response and a near-complete response on PET scan more than 9 months after the start of the treatment (Fig. 4f). Given the small sample size of this phase 1b trial, we must guard against general conclusions about the efficacy of this combination treatment, and a larger phase II trial expansion is planned to evaluate the potential benefit of adding dupilumab to checkpoint blockade in patients progressing on standard immunotherapy,

and to identify biomarkers of patients in whom disrupting the IL-4Rα signalling may be of clinical utility.

Discussion

Tumour-infiltrating monocytes and macrophages have long been considered drivers of immunosuppression and cancer progression; however, so far all therapies targeting these cell types have failed in the clinic[54], primarily because we lack a fundamental understanding of the key regulators of myeloid programmes in tumours, as well as the heterogeneity within and between patients. Here, we define IL-4 as a central driver controlling monocyte and mo-mac immunosuppression in NSCLC, and find that the relevant site of IL-4 signalling is not the tumour itself, but the bone marrow, where it acts on GMPs to imprint myeloid cell fate. Although our mouse models relied on orthotopic transplantation of tumour cells and therefore may mimic some features of lung metastasis, we have previously shown that KP tumours histologically, cellularly and immunologically resemble primary human NSCLC lesions[9,11]. Nevertheless, defining how dupilumab administration modulates the antitumour immune response at different stages of human lung cancer remains an important and exciting area for future study.

Although we found IL-4 expression to be relatively low in lung tumours, our study does not preclude a role for local IL-4 signalling in NSCLC. Indeed, low levels of IL-4-competent CD4 T cells (Extended Data Fig. 4b,c) and eosinophils (Fig. 3c) are present in NSCLC tumours and may modulate the TME in ways that are not addressed in this study. These cell types may be expanded in certain subsets of patients and contribute to inter-patient TME heterogeneity. Additionally, other tumour types, such as pancreatic ductal adenocarcinoma[55] and breast cancer[56] are well-described to be highly T_H2-biased and may serve as paradigms of IL-4 having a major signalling role within the TME. However, in relation to the monocyte–mo-mac lineage in NSCLC, our study clearly points to an extratumoral role for IL-4 signalling in determining tumour outcome. It also highlights that cancer contributes to a systemic dysregulation of the immune system that requires a deep understanding and therapeutic strategies beyond the primary site of disease. Owing to its ability to control immunosuppressive myelopoiesis—a prominent feature of essentially all cancers—we surmise that dupilumab may be an effective combination therapy for many tumour types, that should be explored in the future.

Online content

Any methods, additional references, Nature Portfolio reporting summaries, source data, extended data, supplementary information, acknowledgements, peer review information; details of author contributions and competing interests; and statements of data and code availability are available at https://doi.org/10.1038/s41586-023-06797-9.

1. Barry, S. T., Gabrilovich, D. I., Sansom, O. J., Campbell, A. D. & Morton, J. P. Therapeutic targeting of tumour myeloid cells. *Nat. Rev. Cancer* **23**, 216–237 (2023).
2. Castro, M. et al. Dupilumab efficacy and safety in moderate-to-severe uncontrolled asthma. *N. Engl. J. Med.* **378**, 2486–2496 (2018).
3. Rabe, K. F. et al. Efficacy and safety of dupilumab in glucocorticoid-dependent severe asthma. *N. Engl. J. Med.* **378**, 2475–2485 (2018).
4. Simpson, E. L. et al. Two phase 3 trials of dupilumab versus placebo in atopic dermatitis. *N. Engl. J. Med.* **375**, 2335–2348 (2016).
5. Beck, K. M., Yang, E. J., Sekhon, S., Bhutani, T. & Liao, W. Dupilumab treatment for generalized prurigo nodularis. *JAMA Dermatol.* **155**, 118–120 (2019).
6. Herbst, R. S., Morgensztern, D. & Boshoff, C. The biology and management of non-small cell lung cancer. *Nature* **553**, 446–454 (2018).
7. Lavin, Y. et al. Innate immune landscape in early lung adenocarcinoma by paired single-cell analyses. *Cell* **169**, 750–765.e717 (2017).
8. Leader, A. M. et al. Single-cell analysis of human non-small cell lung cancer lesions refines tumor classification and patient stratification. *Cancer Cell* **39**, 1594–1609.e1512 (2021).
9. Casanova-Acebes, M. et al. Tissue-resident macrophages provide a pro-tumorigenic niche to early NSCLC cells. *Nature* **595**, 578–584 (2021).
10. Loyher, P. L. et al. Macrophages of distinct origins contribute to tumor development in the lung. *J. Exp. Med.* **215**, 2536–2553 (2018).
11. Maier, B. et al. A conserved dendritic-cell regulatory program limits antitumour immunity. *Nature* **580**, 257–262 (2020).
12. Park, M. D. et al. TREM2 macrophages drive NK cell paucity and dysfunction in lung cancer. *Nat. Immunol.* **24**, 792–801 (2023).
13. Loschko, J. et al. Absence of MHC class II on cDCs results in microbial-dependent intestinal inflammation. *J. Exp. Med.* **213**, 517–534 (2016).
14. Karasawa, K. et al. Vascular-resident CD169-positive monocytes and macrophages control neutrophil accumulation in the kidney with ischemia-reperfusion injury. *J. Am. Soc. Nephrol.* **26**, 896–906 (2015).
15. Lee, P. P. et al. A critical role for Dnmt1 and DNA methylation in T cell development, function, and survival. *Immunity* **15**, 763–774 (2001).
16. Liu, Z. et al. Fate mapping via Ms4a3-expression history traces monocyte-derived cells. *Cell* **178**, 1509–1525 e1519 (2019).
17. Horton, B. L. et al. Lack of $CD8^+$ T cell effector differentiation during priming mediates checkpoint blockade resistance in non–small cell lung cancer. *Sci. Immunol.* **6**, eabi8800 (2021).
18. Burger, M. L. et al. Antigen dominance hierarchies shape $TCF1^+$ progenitor CD8 T cell phenotypes in tumors. *Cell* **184**, 4996–5014.e4926 (2021).
19. Chihara, N. et al. Induction and transcriptional regulation of the co-inhibitory gene module in T cells. *Nature* **558**, 454–459 (2018).
20. Khan, O. et al. TOX transcriptionally and epigenetically programs $CD8^+$ T cell exhaustion. *Nature* **571**, 211–218 (2019).
21. Naluyima, P. et al. Terminal effector CD8 T cells defined by an $IKZF2^+IL\text{-}7R^-$ transcriptional signature express FcγRIIIA, expand in HIV infection, and mediate potent HIV-specific antibody-dependent cellular cytotoxicity. *J Immunol* **203**, 2210–2221 (2019).
22. Akimova, T., Beier, U. H., Wang, L., Levine, M. H. & Hancock, W. W. Helios expression is a marker of T cell activation and proliferation. *PLoS ONE* **6**, e24226 (2011).
23. Thome, M. Multifunctional roles for MALT1 in T-cell activation. *Nat. Rev. Immunol.* **8**, 495–500 (2008).
24. Yona, S. et al. Fate mapping reveals origins and dynamics of monocytes and tissue macrophages under homeostasis. *Immunity* **38**, 79–91 (2013).
25. Passegue, E., Wagner, E. F. & Weissman, I. L. JunB deficiency leads to a myeloproliferative disorder arising from hematopoietic stem cells. *Cell* **119**, 431–443 (2004).
26. Abram, C. L., Roberge, G. L., Hu, Y. & Lowell, C. A. Comparative analysis of the efficiency and specificity of myeloid-Cre deleting strains using ROSA-EYFP reporter mice. *J. Immunol. Methods* **408**, 89–100 (2014).
27. Mohrs, M., Shinkai, K., Mohrs, K. & Locksley, R. M. Analysis of type 2 immunity in vivo with a bicistronic IL-4 reporter. *Immunity* **15**, 303–311 (2001).
28. Hanna, R. N. et al. The transcription factor NR4A1 (Nur77) controls bone marrow differentiation and the survival of $Ly6C^-$ monocytes. *Nat. Immunol.* **12**, 778–785 (2011).
29. Kurotaki, D. et al. Transcription factor IRF8 governs enhancer landscape dynamics in mononuclear phagocyte progenitors. *Cell Rep.* **22**, 2628–2641 (2018).
30. Zhao, F. et al. S100A9 a new marker for monocytic human myeloid-derived suppressor cells. *Immunology* **136**, 176–183 (2012).
31. Hegde, S., Leader, A. M. & Merad, M. MDSC: markers, development, states, and unaddressed complexity. *Immunity* **54**, 875–884 (2021).
32. Seita, J. & Weissman, I. L. Hematopoietic stem cell: self-renewal versus differentiation. *Wiley Interdiscip. Rev. Syst. Biol. Med.* **2**, 640–653 (2010).
33. Yanez, A. et al. Granulocyte-monocyte progenitors and monocyte-dendritic cell progenitors independently produce functionally distinct monocytes. *Immunity* **47**, 890–902 e894 (2017).
34. Mastio, J. et al. Identification of monocyte-like precursors of granulocytes in cancer as a mechanism for accumulation of PMN-MDSCs. *J. Exp. Med.* **216**, 2150–2169 (2019).
35. Nelms, K., Keegan, A. D., Zamorano, J., Ryan, J. J. & Paul, W. E. The IL-4 receptor: signaling mechanisms and biologic functions. *Annu. Rev. Immunol.* **17**, 701–738 (1999).
36. Jenkins, S. J. et al. Local macrophage proliferation, rather than recruitment from the blood, is a signature of T_H2 inflammation. *Science* **332**, 1284–1288 (2011).
37. Paul, F. et al. Transcriptional heterogeneity and lineage commitment in myeloid progenitors. *Cell* **163**, 1663–1677 (2015).
38. Kwok, I. et al. Combinatorial single-cell analyses of granulocyte-monocyte progenitor heterogeneity reveals an early uni-potent neutrophil progenitor. *Immunity* **53**, 303–318. e305 (2020).
39. Olsson, A. et al. Single-cell analysis of mixed-lineage states leading to a binary cell fate choice. *Nature* **537**, 698–702 (2016).
40. Anderson, K. G. et al. Intravascular staining for discrimination of vascular and tissue leukocytes. *Nat. Protoc.* **9**, 209–222 (2014).
41. Tsutsui, H. et al. The basophil-specific protease mMCP-8 provokes an inflammatory response in the skin with microvascular hyperpermeability and leukocyte infiltration. *J. Biol. Chem.* **292**, 1061–1067 (2017).
42. Cohen, M. et al. Lung single-cell signaling interaction map reveals basophil role in macrophage imprinting. *Cell* **175**, 1031–1044.e1018 (2018).
43. Obata, K. et al. Basophils are essential initiators of a novel type of chronic allergic inflammation. *Blood* **110**, 913–920 (2007).
44. Schultze, J. L., Mass, E. & Schlitzer, A. Emerging principles in myelopoiesis at homeostasis and during infection and inflammation. *Immunity* **50**, 288–301 (2019).
45. Veglia, F., Sanseviero, E. & Gabrilovich, D. I. Myeloid-derived suppressor cells in the era of increasing myeloid cell diversity. *Nat. Rev. Immunol.* **21**, 485–498 (2021).
46. Pellefigues, C. et al. Diverse innate stimuli activate basophils through pathways involving Syk and IkappaB kinases. *Proc. Natl Acad. Sci. USA* **118**, e2019524118 (2021).
47. Gandhi, L. et al. Pembrolizumab plus chemotherapy in metastatic non-small-cell lung cancer. *N. Engl. J. Med.* **378**, 2078–2092 (2018).
48. Spigel, D. R. et al. Five-year survival outcomes from the PACIFIC trial: durvalumab after chemoradiotherapy in stage III non-small-cell lung cancer. *J. Clin. Oncol.* **40**, 1301–1311 (2022).
49. Herbst, R. S. et al. Five year survival update from KEYNOTE-010: pembrolizumab versus docetaxel for previously treated, programmed death-ligand 1-positive advanced NSCLC. *J. Thorac. Oncol.* **16**, 1718–1732 (2021).

50. Choi, H. et al. Transcriptome analysis of individual stromal cell populations identifies stroma–tumor crosstalk in mouse lung cancer model. *Cell Rep.* **10**, 1187–1201 (2015).
51. Patil, N. S. et al. Intratumoral plasma cells predict outcomes to PD-L1 blockade in non-small cell lung cancer. *Cancer Cell* **40**, 289–300.e284 (2022).
52. Petitprez, F. et al. B cells are associated with survival and immunotherapy response in sarcoma. *Nature* **577**, 556–560 (2020).
53. Eisenhauer, E. A. et al. New response evaluation criteria in solid tumours: revised RECIST guideline (version 1.1). *Eur. J. Cancer* **45**, 228–247 (2009).
54. Anderson, N. R., Minutolo, N. G., Gill, S. & Klichinsky, M. Macrophage-based approaches for cancer immunotherapy. *Cancer Res.* **81**, 1201–1208 (2020).
55. Alam, A. et al. Fungal mycobiome drives IL-33 secretion and type 2 immunity in pancreatic cancer. *Cancer Cell* **40**, 153–167.e111 (2022).
56. DeNardo, D. G. et al. CD4$^+$ T cells regulate pulmonary metastasis of mammary carcinomas by enhancing protumor properties of macrophages. *Cancer Cell* **16**, 91–102 (2009).

Publisher's note Springer Nature remains neutral with regard to jurisdictional claims in published maps and institutional affiliations.

Springer Nature or its licensor (e.g. a society or other partner) holds exclusive rights to this article under a publishing agreement with the author(s) or other rightsholder(s); author self-archiving of the accepted manuscript version of this article is solely governed by the terms of such publishing agreement and applicable law.

© The Author(s), under exclusive licence to Springer Nature Limited 2023

[1]Marc and Jennifer Lipschultz Precision Immunology Institute, Icahn School of Medicine at Mount Sinai, New York, NY, USA. [2]The Tisch Cancer Institute, Icahn School of Medicine at Mount Sinai, New York, NY, USA. [3]Department of Immunology and Immunotherapy, Icahn School of Medicine at Mount Sinai, New York, NY, USA. [4]Columbia Stem Cell Initiative, Department of Genetics and Development, Columbia University, New York, NY, USA. [5]Division of Hematology/Oncology, Icahn School of Medicine at Mount Sinai, New York, NY, USA. [6]Center for Thoracic Oncology, Icahn School of Medicine at Mount Sinai, New York, NY, USA. [7]Singapore Immunology Network (SIgN), Agency for Science, Technology and Research (A*STAR), BIOPOLIS, Singapore, Singapore. [8]INSERM U1015, Gustave Roussy Cancer Campus, Villejuif, France. [9]Shanghai Institute of Immunology, Shanghai Jiao Tong University School of Medicine, Shanghai, China. [10]SingHealth Duke-NUS Academic Medical Centre, Translational Immunology Institute, Singapore, Singapore. [11]Human Immune Monitoring Center, Icahn School of Medicine at Mount Sinai, New York, NY, USA. [12]Inflammation, Infection and Immunity Laboratory, Advanced Research Institute, Tokyo Medical and Dental University (TMDU), Tokyo, Japan. [13]Icahn Genomics Institute, Icahn School of Medicine at Mount Sinai, New York, NY, USA. [14]Kimberly and Eric J. Waldman Department of Dermatology, Icahn School of Medicine at Mount Sinai, New York City, NY, USA. [15]Mark Lebwohl Center for Neuroinflammation and Sensation, Icahn School of Medicine at Mount Sinai, New York City, NY, USA. [16]Friedman Brain Institute, Icahn School of Medicine at Mount Sinai, New York City, NY, USA. [17]Present address: CeMM Research Center for Molecular Medicine of the Austrian Academy of Sciences, Vienna, Austria. [18]These authors contributed equally: Samarth Hegde, Matthew D. Park. [19]These authors jointly supervised this work: Thomas U. Marron and Miriam Merad. ✉e-mail: miriam.merad@mssm.edu

Methods

Mice

C57BL/6 mice were obtained from Charles River Laboratories. *Zbtb46-cre* (strain 028538), *CD4-cre* (strain 022071), *S100a8-cre* (strain 021614), *Cx3cr1-cre* (strain 025524) and CD45.1 (strain 002014) were obtained from Jackson Laboratories. *CD169-cre* mice were a gift from P. Frenette. *Ms4a3-cre* mice were a gift from F. Ginhoux. *Il4*-eGFP (4get) mice fully backcrossed to the C57BL/6 background were obtained from B.S.K. *Il4ra*-floxed mice were generated by Cyagen. In brief, CRISPR–Cas9 editing was used to generate mice with *loxP* sites flanking exon 4 of the *Il4ra* gene, located on mouse chromosome 7. Both male and female mice were used, and we observed no differences between sexes in any experiment. Littermate controls were used in all experiments, with the single exception of Extended Data Fig. 1h, where sex and age-matched controls were used. All experiments were initiated when mice were between 8 and 12 weeks of age. Investigators were not blinded to mouse groups. No statistical methods were used to determined sample size. Adequate sample size was determined based on reproduciblility between experiments. Mice were housed in specific-pathogen free conditions at 21–22 °C at 39–50% humidity with a 12/12 h dark/light cycle. Mice were euthanized by CO_2 asphyxiation. All experiments were approved by, and in compliance with, the Institutional Animal Care and Use Committee of the Icahn School of Medicine at Mount Sinai.

Lung tumour models

In total, 500,000 KP cells (obtained from T. Jacks), 150,000 HKP1 cells (obtained from V. Mittal) or 500,000 B16 cells (obtained from the American Type Culture Collection) were injected intravenously through the tail vein in 300 µl of sterile normal saline. In most cases, GFP-expressing KP cells were used. If mice expressed endogenous GFP (such as *IL4*-eGFP 4get mice), then KP cells lacking GFP were used. Mice were heated with a heat lamp for 5 min prior to intravenous injection. Mice were euthanized at 28 days post KP injection, 17 days post HKP1 injection, or 15 days post B16 injection (±2 days). Mouse cohorts were euthanized at earlier timepoints (not more than 5 days) if mice showed clinical signs of distress requiring a humane end point (laboured breathing, hunched posture or wasting). All cell lines were routinely screened for mycoplasma contamination. All tumour experiments were replicated multiple times on different days using separately thawed vials of cells. After thawing, cells were not passaged more than five times prior to injection and cells were only injected if they were at >90% viability. All cell lines were maintained at 37 °C in RPMI (Corning, 10–040-CV) supplemented with 10% fetal bovine serum (FBS) (Gibco, A52568-01) and 1% penicillin/streptomycin (pen/strep) (ThermoFisher, 15140163). Cells were injected at 70% confluency after 10 min of trypsinization at 37 °C (Gibco, 25200-056), washing with sterile PBS, and filtering through 70-µm filters.

Antibody and antibody complex treatments

Relevant isotype antibodies were used in control groups for all antibody experiments. Where indicated, mice were treated with 25 µg of anti-IL-4 (BioXcell, clone 11B11, BE0045) intraperitoneally on days 21, 23 and 26 post KP injection and analysed on day 28; 25 µg of anti-IL-4 on days 8, 10 and 13 and analysed on day 23; 10 µg anti-FCER1A (ThermoFisher, clone MAR-1, 14-5898) intraperitoneally on days −3, 3, 7, 14 and 21 post KP injection and analysed on day 25; 50 µg of anti-CD200R3 (H.K. laboratory, clone Ba103) intravenously on days 2, 9, 16 and 23 post KP injection and analysed on day 25. IL-4c was generated as previously described[36]. Mice were injected intraperitoneally with either vehicle control or 5 µg IL-4 (Shenandoah, 200-18) complexed to 25 µg of anti-IL-4 on days 0 and 2 and analysed on day 4. For combinatorial PD-L1–IL-4 blockade, two similar experiments using the HKP1 tumour cell line were combined. In experiment 1, 200 µg anti-PD-L1 (BioXcell, clone 10 F.9G2, BE0101) was given on day 9 and/or 25 µg anti-IL-4 was given on days 7, 9, 11 and 14, and mice were euthanized on day 17. In experiment 2, 200 µg anti-PD-L1 was given on day 11, and/or 25 µg anti-IL-4 was given on day 11, 13 and 15, and mice were euthanized on day 17.

In vivo labelling of circulating immune cells

To distinguish parenchymal from circulating immune cells, mice were injected intravenously with 3 µg of fluorescently labelled CD45 antibodies in 100 µl of saline. Three minutes later, mice were euthanized and CD45 intravenous labelling in immune compartments was analysed by flow cytometry.

Bone marrow transplant

Lethally irradiated (2 × 6.5 Gy) 8- to 12-week-old wild-type CD45.1 mice were reconstituted with a 1:1 ratio of wild-type CD45.1 and *Il4ra*$^{\Delta Ms4a3}$ CD45.2 bone marrow cells (5×10^6 cells of each genotype) retro-orbitally. Mice were kept on sulfamethoxazole–trimethoprim for 3 weeks. Mice were analysed 12 weeks after reconstitution.

Mouse lung histology

One lung lobe per mouse was fixed overnight in 4% paraformaldehyde before being stored in 70% ethanol until further processing. Lungs were sectioned 4 µm thick formalin-fixed paraffin-embedded (FFPE) tissue sections, and stained with haematoxylin and eosin (H&E). All sectioning and staining was performed by the Histopathology Core Facility of the Department of Oncological Sciences at the Icahn School of Medicine at Mount Sinai. Slides were scanned at 20× using a Leica Aperio AT2 Digital Scanner and tumour burden was quantified using Qupath software.

Tissue processing

Mouse lungs were minced with scissors and digested in 2 ml of 0.25 mg ml^{-1} Collagenase IV (Sigma, C5138-1G) in RPMI for 30 min at 37 °C before being aspirated through an 18 G needle and passaged through 70-µm filters. Bone marrow was flushed from leg long bones (femur and tibia) and passaged through 70-µm filters. Blood was collected from inferior vena cava. Red blood cells from all tissues were lysed with ACK Lysis Buffer (BioLegend, 420301) for 3 min at room temperature prior to downstream processing.

Flow cytometry and fluorescence-activated cell sorting

Single cells were resuspended in fluorescence-activated cell sorting (FACS) buffer (phosphate-buffered saline (PBS) (Sigma Aldrich, D8537-6X500ML) supplemented with 2% bovine serum albumin (Equitech-Bio, BAH62-0500) and 5 mM EDTA). Cells were surface-stained for 15 min on ice. For intracellular cytokine staining, cells were fixed with Cytofix/Cytoperm (BD, 554722), and then stained for intracellular antigens in permeabilization buffer (BD, 554723). For pSTAT6 staining, surface-stained cells were fixed at room temperature for 10 min in 4% paraformaldehyde and then further fixed in methanol at −80 °C for 1 h. Finally, cells were intracellularly stained in PBS containing 0.1% bovine serum albumin and 0.5% Triton X-100. For cytokine staining, cells were first simulated in 10 µg ml^{-1} Brefeldin A, 0.5 µg ml^{-1} Ionomycin and 0.2 µg ml^{-1} phorbol myristate acetate for 4 h at 37 °C. Dead cells were excluded by using 4′,6-diamidino-2-phenylindol (DAPI) (ThermoFisher, D1306) or Fixable Blue Live/Dead Dye (Fisher Scientific, L23105). Stained cells were acquired on a BD LSRFortessa Cell Analyzer or sorted on a BD FACSAria. Data were analysed using FlowJo v10 software. The following anti mouse FACS antibodies were used in this study: CD45 (clone 30-F11, Biolegend, 103138, 1:100), IL-4Rα (clone I015F8, Biolegend, 144805, 1:100), IL-4 (clone 11B11, ThermoFisher, 17-7041-81, 12-7041-82, 1:100), IL-12p40 (clone C17.8, ThermoFisher, 505211, 1:100), CD103 (clone 2E7, Biolegend, 13-1031-82, 1:100), CD11b (clone M1/70, Biolegend 101230, ThermoFisher 47-0112-82, 1:200), CD11c (clone N418, Biolegend, 117336, 1:400), CD127 (clone A7R34, Biolegend, 135019, 1:100), CD4 (clone RM4-5, Biolegend, 100545, 1:200), CD8α (clone 53-6.7, Biolegend, 100714, 1:200), CD3 (clone 17A2,

ThermoFisher, 47-0032-82, 1:200), CX3CR1 (clone SA011F11, Biolegend, 149023, 1:200), LY6G (clone 1A8, 127624, Biolegend, 1:200), LY6C (clone HK1.4, Biolegend 128035, Thermofisher 17-5932-82, 1:400), TCRβ (clone H57-597, Biolegend, 109228, 1:400). SIGLECF (clone E50-2440, BD Pharmingen, 562680, 565527, 1:100), MHC II I-A/I-E (clone M5/114.15.2, Biolegend, 107643, 1:400), CD115 (clone AFS98, eBioscience, 17-1152-82, 13-1152-85, 1:100), CD2 (clone RM2-4, Biolegend, 100114, 1:200), MerTK (clone DS5MMER, eBioscience, 12-5751-82, 1:100), CD64 (clone X54-5/7.1, ThermoFisher 17-0641-82, Biolegend 139318, 1:100), CD16/CD32 (clone 93, ThermoFisher, 56-0161-82, 1:300), CD34 (clone HM34, Biolegend, 128612; clone RAM34, ThermoFisher, 48-0341-82, 1:100), c-kit (clone 2B8, Biolegend 553353, ThermoFisher 25-1171-82, 1:100), ST2 (clone RMST2-2, ThermoFisher, 46-9335-82, 1:100), SCA-1 (clone D7, ThermoFisher, 25-0981-81, Biolegend 108126, 1:100), CD150 (clone mShad150, ThermoFisher, 17-1502-80, 1:100), CD48 (clone HM48-1, ThermoFisher, 46-0481-80, 1:100), CD135 (clone A2F10, Biolegend, 135306, 1:50), NK1.1 (clone PK136, Biolegend 108724, ThermoFisher 45-5941-82, 1:100), CD19 (clone eBio1D3, ThermoFisher, 48-0193-82, 1:200), TER-119 (clone Ter-119, ThermoFisher, 47-5921-82, 1:200), B220 (clone RAB-632, ThermoFisher, 47-0452-82, 1:200), FCER1A (clone MAR-1, Biolegend, 134308, 1:100), CD49b (clone DX5, eBioscience, 48-5971-82, 1:100), ARG-1 (clone A1exF5, eBioscience, 53-3697-82, 1:100), F4/80 (clone BM8, ThermoFisher, 48-4801-82, 1:200), CD200R3 (Clone Ba13, Biolegend, 142205, 1:100), CD86 (clone GL-1, Biolegend, 105006, 1:100), pSTAT6 (Tyr641) (clone CHI2S4, eBioscience, 17-9013-42, 1:100), CD90.2 (clone 30-H12, ThermoFisher, 25-0902-81, 1:200), CD45.2 (clone 104, Biolegend 109830, ThermoFisher 47-0454-82, 1:200), CD45.1 (clone A20, Biolegend, 110741, 1:200), PD-L1 (clone MIH5, ThermoFisher, 12-5982-82, 1:200), CD206 (clone C068C2, Biolegend, 141703, 1:200). Gating strategies can be found in Extended Data Figs. 5f and 6a, and all gating strategies not explicitly referenced can be found in Extended Data Fig. 7a.

BMDM differentiation

Wild-type C57BL/6 bone marrow was plated on non-tissue culture-treated plates at a concentration of 150,000 cells per cm^2 in DMEM (Corning, 10-013-CV) containing 10% FBS, 1% pen/strep and 10 ng ml^{-1} M-CSF (Peprotech, 315-03) or 10 ng ml^{-1} M-CSF plus 200 ng ml^{-1} IL-4. After 2 days, nonadherent cells were replated on new plates containing complete DMEM with M-CSF, and medium was replenished every 2 days thereafter until day 7, at which time BMDMs were polarized overnight with indicated cytokines. BMDMs were then lifted off plates with cold PBS containing EDTA and analysed by flow cytometry. BMDMs were identified as live cells co-expressing F4/80 and CD11b, representing more than 95% of all cells in each experiment.

Tumour-conditioned medium

Tumour-conditioned medium was generated by plating KP cells in 25 ml RPMI with 10% FBS and 1% pen/strep in a 175-cm^2 flask (Fisher Scientific, 12-562-000) at 50% confluency. One day later, when cells were near 100% confluency medium was removed, centrifuged at 1400 rpm for 5 min to remove cells, and stored at −20 °C until further use.

Bone marrow co-cultures

In total, 3×10^5 red blood cell lysed bone marrow cells from 4get mice were cultured for two days 96 well plates in 200 µl of control medium (RPMI plus 10% FBS and 1% pen/strep) or in tumour-conditioned medium or in the presence of the following mouse cytokines: CCL3 (Peprotech, 250-09), Csf2 (Peprotech, 315-03), IL-1α (R&D Systems, 400-ML-005/CF), IL-6 (Peprotech, 216-16), IL-7 (Peprotech, 217-17), IL-15 (Peprotech, 210-15), IL-18 (R&D Systems, 9139-IL-010/CF) or VEGF-A (Peprotech, 450-32). Tumour-conditioned medium was used undiluted. Indicated cytokines were cultured at decreasing concentrations-100 ng ml^{-1}, 10 ng ml^{-1} and 1 ng ml^{-1}. All cytokines were first resuspended in cell culture grade water at a concentration of 0.1 mg ml^{-1} and then diluted in RPMI immediately before culture. Basophils were identified per the gating strategy in Extended Data Fig. 6a and *IL4*-eGFP expression was measured by flow cytometry via the FITC channel. In parallel, all experiments were performed with bone marrow from wild-type mice to rule out any effect of autofluorescence; these control experiments showed no difference in GFP/FITC mean fluorescence intensity between any experimental conditions. No alteration in cell viability was observed in any experimental condition.

Methylcellulose assay

Total haematopoietic cells were extracted from $Il4ra^{+/+}$ and $Il4ra^{\Delta Ms4a3}$ bone marrow by flushing one femur and one tibia with PBS, red blood cell lysed and cells resuspended to a concentration of 3×10^5 cells per ml in IMDM (Cytivia, SH30228.01) containing 1% pen/strep and 2% FBS. Cytokines as indicated in figures were added at a 10× concentration (100 ng ml^{-1}). A volume of 0.4 ml of the resultant cells was added to pre-aliquoted 4 ml StemCell MethoCult M3434 tubes (already containing recombinant mouse (rm)SCF, rmIL3, rmIL6, recombinant human (rh)EPO, rhInsulin and transferrin). The MethoCult was vortexed and dispensed onto 35-mm culture dishes in triplicates following manufacturer's instructions. The dishes were incubated in a humidified incubator at 37 °C, 5% CO_2. Colonies were manually counted on day 8 on a Gridded Scoring Dish and averaged across 3 or 4 plates.

CyTOF

Our CyTOF pipeline has been described in detail elsewhere[7]. In brief, immune cells from whole blood first were barcoded with antibodies specific to CD45. Then, samples were combined together and stained with a customized panel of metal-conjugated antibodies. Samples were washed, fixed, and stored at 4 °C until acquisition. Samples were acquired on a CyTOF2 (Fluidigm), and data were normalized using CyTOF software (bead-based normalization). Samples were debarcoded using the Fluidigm debarcoding software. Immune cell populations were quantified using FlowJo v10 software. A gating strategy can be found in Extended Data Fig. 7b. A list of CyTOF antibodies and metal conjugates can be found in Supplementary Table 7.

Multiplexed cytokine assays

Mouse lung homogenate was analysed with Multiplex Luminex Assay (Millipore). Plasma from our clinical trial cohort, treatment-naive patients with NSCLC, and healthy control donors analysed using the Olink proteomic array, and differential protein abundance was calculated using R Studio. Control plasma was obtained from de-identified healthy donors (IRB 11-00866). Serum from patients with NSCLC was obtained via IRB 10-00472 A. Both of these assays were performed by trained staff at the Human Immune Monitoring Center at the Icahn School of Medicine at Mount Sinai.

Immunohistochemistry

Our multiplexed immunohistochemical consecutive staining on a single slide (MICSSS) protocol has been described in detail elsewhere[57]. In brief, biopsies were fixed overnight in 4% paraformaldehyde and embedded in paraffin, and 4-µm sections were cut onto charged glass slides. Slides were baked at 37 °C overnight, deparaffinized in xylene, and rehydrated in ethanol. Antigen retrieval occurred for 30 min in citrate buffer (pH 6) (Agilent, S236984) or EDTA buffer (pH 9) (Agilent, S236784) at 95 °C using a water bath. Tissues were blocked in 3% hydrogen peroxide and protein block solution (Dako, X0909), followed by staining with primary antibodies according to their optimized dilutions and secondary antibodies conjugated to horseradish peroxidase (Agilent Technologies, K400111-2, K400311-2). Chromogenic revelation was performed with 3-amino-9-ethylcarbazole (AEC) (Vector Laboratories, SK4200). After mounting, slides were scanned at 40× on a Leica Aperio AT2 Digital Scanner. Slides were destained and restained with new antibodies as previously described until the entire antibody

panel was completed. Tumour area was identified by a pathologist and cells staining positive for indicated markers were quantified manually using Qupath software. For mouse CD8 T cell quantification in tumours, samples were stained in a similar manner and CD8-positive cells were quantified using automated cell detection with Qupath software. A complete list of antibodies and staining conditions can be found in Supplementary Table 8. As a positive control for MCP-8 basophil staining, we used FFPE sections of ear skin from mice that underwent the classical MC903 model of atopic dermatitis donated by B.S.K.[58].

For multiplexed imaging, we internally processed our samples to quantitatively analyse localization and coexpression patterns from MICSSS images. For the analysis, we used the svs multi-resolution, pyramidal images obtained per marker after staining. Each image underwent a brief quality control step to ensure tissue masking appropriately captured the tissue area. Both the AEC chromogen stain and the haematoxylin nuclear counterstain were extracted from each image via a dynamically determined deconvolution matrix. Then, each image was split into smaller tiles to permit computational analysis. Each tile from the first stained image was matched to the respective tile from the sequential stained images and then elastically registered using the extracted haematoxylin nuclear stain and SimpleElastix open-source software. Then, by using an iterative nuclear masking via STARDIST, we produced a composite semantic segmentation for nuclei residing in the series of tiles. Each nucleus was artificially expanded by a number of pixels to simulate a cytoplasm per cell and that was coherent with membrane marker staining. Lastly, cellular-resolution metadata was acquired for all cells in the final cell mask, including AEC and haematoxylin intensity properties (percentiles, dynamic ranges, and so on) and morphological characteristics (circularity, area, and so on) per cell. A final data frame was appended for each tile processed, producing one data frame representing all the cellular metadata per sample.

To unbiasedly determine positive and negative cells per marker, we used an unsupervised classification technique to cluster cell populations, followed by a supervised approach where we would evaluate each cluster as positive or negative per marker. First, the metadata aggregated per sample was collected, transformed to *z*-scores, randomized, and split into subsamples per batch. Each batch was processed in parallel: data for each marker was transformed, clustered and collapsed into multiple groups by principal components analysis and uniform manifold approximation and projection. Then, we performed the final quality control to manually attribute which clusters were positive or negative. This produced a final cellular-resolution data frame containing binary marker classification that was used for downstream localization, marker coexpression, tumour annotation and reconciliation and statistical analyses.

Immunofluorescence on bone marrow sections

Mouse femurs were snap frozen in OCT (Tissue-Tek) and kept at −80 °C until sectioning. The sections were prepared at 7 µm using a Cryostat with tungsten blades and the Cryojane tape transfer system, dried overnight at room temperature and stored at −80 °C until staining. To fix and permeabilize the sections, the slides were incubated in 100% acetone for 10 min at −20 °C. For basophil staining, anti-FCER1A (MAR-1, ThermoFisher 14-5898-82) was used at 1:200 dilution and followed by goat anti-Armenian hamster IgG conjugated to A488 (Jackson ImmunoResearch, 127-545-160) at 1:500 dilution. For myeloid progenitor staining, anti-CD117 (ACK2, Biolegend 135102) was used at 1:25 dilution and followed by goat anti-rat Cy3 (Jackson Immunoresearch, 112-165-167) at 1:100 dilution. For lineage staining, a combination of anti-Mac1 (M1/70, Biolegend 101218), anti-Gr1 (RB6-8C5, Biolegend 108418), anti-B220 (RA3-6B2, Biolegend 103226), anti-CD3 (17A2, Biolegend 100209), anti-CD150 (TC15-12F12.2, Biolegend 115918), anti-SCA-1 (D7, Biolegend 108118) all directly conjugated to A647 and at 1:100 dilution was used. The sections were blocked using 10% goat serum (Gibco 16210064) at room temperature for 1 h when goat secondary antibodies were used or 1:50 Rat IgG (Sigma Aldrich, I8015) at room temperature for 10 min when lineage antibodies were used. The sections were then incubated with primary antibodies overnight at 4 °C. The incubation with secondary antibodies was done at room temperature for 1.5 h. Several washing steps were performed after each antibody. The sections were mounted with Prolong Glass Antifade Mountant (ThermoFisher P36980) and imaged with a SP8 inverted confocal microscope (Leica) with 20× objective across *z*-stacks. Images were processed with ImageJ.

scRNA-seq

For all mouse scRNA-seq analyses, three mice were analysed per condition. For scRNA-seq of KP tumour-bearing *Il4ra*$^{+/+}$ and *Il4ra*$^{\Delta Ms4a3}$ lungs, T cells and myeloid cells were separately sorted and barcoded with 10x Cellplex oligos before being encapsulated using the 10X Chromium 3′ v3 Chemistry Kit according to manufacturer's instructions. Cells sorted from the same genotype were barcoded and pooled into individual lanes. A total of 12,000 cells were loaded per lane from each condition. For scRNA-seq of bone marrow of naive, tumour-bearing and IL-4c treated mice, bone marrow myeloid cells and were sorted for sequencing. Due to their abundance in bone marrow, neutrophils were separately sorted and then recombined back with the above cells at a 1:10 ratio. Sorting strategies for all sequencing experiments can be found in Extended Data Fig. 8a,b. Cells sorted from the same genotype were barcoded and pooled into individual lanes. A total of 12,000 cells were loaded per lane from each condition. All sequencing libraries were prepared per manufacturer instructions. After stringent cDNA and sequencing library quality control with the CybrGreen qPCR library quantification assay, samples were sequenced at a depth of 100 million reads per library with a 75-cycle kit on an Illumina Nextseq 550. For human scRNA-seq analysis, our previously published dataset of leukocytes from tumour and adjacent normal lung of 35 treatment-naive patients with NSCLC[8] was queried.

scRNA-seq downstream analysis

Gene expression reads were aligned to the mm10 reference transcriptome followed by count matrix generation using the default CellRanger 2.1 workflow, using the 'raw' matrix output. Following alignment, barcodes matching cells that contained >500 unique molecular identifiers (UMIs) were extracted. From these cells, those with transcripts >25% mitochondrial genes were filtered from downstream analyses. For lung immune cells sorted for scRNA-seq in Fig. 1, a total of 7,400 myeloid cells (4,171 *Il4ra*$^{+/+}$ and 3,229 *Il4ra*$^{\Delta Ms4a3}$) and 9,255 T cells (5,735 *Il4ra*$^{+/+}$ and 3,520 *Il4ra*$^{\Delta Ms4a3}$) passed quality control and were analysed. For bone marrow myeloid cells and progenitors sorted for scRNA-seq in Fig. 2, a total of 22,168 cells passed quality control and were analysed from the following conditions (3 mice per condition): naive: 2,840, 2,574 and 2,276 cells per mouse; IL-4c: 3,399, 2,965 and 2,930 cells per mouse; KP: 1,963, 1,413 and 1,808 cells per mouse. Matrix scaling, logarithmic normalization and batch correction via data alignment through canonical correlation analysis, and unsupervised clustering using a *k*-nearest neighbours graph partitioning approach were performed as previously described[12]. DEGs were identified using the FindMarkers function (Seurat). Mean UMI were imputed to determine logarithmic fold changes in expression between cell states to further the analysis of markers of interest. GSEA was performed using the Enrichr database. Other R packages used include: scDissector v.1.0.0; shiny v.1.7.; ShinyTree v.0.2.7; heatmaply v.1.3.0; plotly v.4.10.0; ggvis v.0.4.7; ggplot2 v.3.3.5; dplyr v.1.0.7; Matrix v.0.9.8; and seriation v.1.3.5. For bar graphs with curated gene lists in Fig. 1d and Extended Data Fig. 1g, genes that had fewer than one UMI in any sample were first excluded. Then the average UMI ratio of *Il4ra*$^{+/+}$ over *Il4ra*$^{\Delta Ms4a3}$ was calculated and filtered to $\log_2 FC > 0.7$ or < -0.7.

Human subjects

Informed consent was obtained from all study participants. Patients with NSCLC that had progressed on standard of care PD-1 or PD-L1 agents were enroled into a clinical trial in which patients received three doses of dupilumab administered subcutaneously (at standard 600 mg loading dose, and subsequently 300 mg every three weeks, for a total of 3 treatments) in conjunction with continued checkpoint blockade. Patients had to have 1 or fewer intervening lines of therapy between PD-1/PD-L1 blockade, an Eastern Cooperative Oncology Group (ECOG) performance status of 2 or better, adequate organ function, and cannot have received chemotherapy within 14 days prior to the start of therapy. Patients with immunodeficiencies, active autoimmune disease or with active viral or bacterial infections were not permitted to enrol. The patient has to be willing to undergo pre-treatment core needle biopsies of their tumour, and repeat biopsies after 4 weeks on treatment (one week following the second administration of dupilumab). Blood was drawn at routine intervals—on the first day of administration, as well as day 4, day 8, day 15, day 22 and day 43 following the start of therapy, and plasma and PBMCs were isolated and cryopreserved for batched analysis. In depth immune phenotyping of tumour and blood, at the proteomic and transcriptomic was prespecified within the trial, which was approved by the Institutional Review Board of Mount Sinai Hospital in accordance with the Declaration of Helsinki. The trial was designed as a Phase 1b/2a clinical trial in which Phase 1b constitutes a set-dose open-label run-in cohort of 6 patients with the primary objective of defining safety and tolerability of this novel combination. Secondary endpoints include best overall response (BORR) as per RECIST v1.1 criteria, progression-free survival (PFS) overall survival (OS) and duration of response (DoR). Plasma was collected from patients at indicated timepoints and analysed by the 96-analyte inflammation panel Olink assay per manufacturer's instructions. All Olink data are reported as linearized normalized protein expression (NPX), per the manufacturer's instructions. Olink assay was performed by trained staff at the Human Immune Monitoring Center at the Icahn School of Medicine at Mount Sinai.

Study participants

We report analysis of specimens from the first six patients that make up the phase Ib run-in for the clinical trial. The patients were evenly split between adenocarcinoma and squamous cell carcinoma, all were male, five out of six were smokers, all but one patient had received prior chemotherapy with or without radiation, and immunotherapy was the most recent treatment received at the time of enrolment. No patients experienced treatment-related adverse events or dose-limiting toxicities as described in the protocol. See Supplementary Table 5 for additional clinical metadata.

Statistics

In all cases where we used parametric statistical tests (that is, Student's *t*-test) we first confirmed that the data were normally distributed using the Anderson–Darling test, D'Agostino and Pearson test, Shapiro–Wilk test, and Klomogorov–Smirnov test, all with an alpha of 0.05. If the data were not normal by any of these tests, then a nonparametric test was used. In cases where more than two groups were compared, an ANOVA with post hoc Tukey's test was performed to determine significance. One statistical outlier was removed in Figs. 1c,f, 2e and 4a with a Grubbs test (Graphpad). For Fig. 1a and Supplementary Table 1, DEGs were run through the Enrichr pipeline[59] and adjusted *P* values were determined by Fisher's exact test. For Extended Data Fig. 5a, DEGs were run through the Metascape pipeline[60] and adjusted *P* values were determined by Fisher's exact test.

Reporting summary

Further information on research design is available in the Nature Portfolio Reporting Summary linked to this article.

Data availability

Raw RNA-seq data have been deposited in the Gene Expression Omnibus (GEO) under accession code GSE245236. Computed tomography images of patients participating in the clinical trial can be downloaded via Amazon Web Services at the following link: https://himc-project-data.s3.amazonaws.com/lamarche_2023/lamarche_image_data.tar.gz?AWSAccessKeyId=AKIAV3HQ5KORNL3V6W43&Signature=N32aM3ouC5FwYvbMvA7eJJd3V4k%3D&Expires=1698691876. Source data are provided with this paper.

Code availability

Code for generating specific figures will be provided by the corresponding author upon reasonable request.

57. Remark, R. et al. In-depth tissue profiling using multiplexed immunohistochemical consecutive staining on single slide. *Sci. Immunol.* **1**, aaf6925 (2016).
58. Wang, F. et al. A basophil–neuronal axis promotes itch. *Cell* **184**, 422–440.e417 (2021).
59. Chen, E. Y. et al. Enrichr: interactive and collaborative HTML5 gene list enrichment analysis tool. *BMC Bioinformatics* **14**, 128 (2013).
60. Zhou, Y. et al. Metascape provides a biologist-oriented resource for the analysis of systems-level datasets. *Nat. Commun.* **10**, 1523 (2019).

Acknowledgements We thank members of the Merad laboratory for thoughtful feedback on the manuscript, members of the Center for Comparative Medicine and Surgery at the Icahn School of Medicine at Mount Sinai for animal husbandry, members of the Human Immune Monitoring Center at the Icahn School of Medicine at Mount Sinai for patient sample processing and scRNA-seq assistance, and all patients who participated in this study and their families. M.M. was partially supported by National Institutes of Health (NIH) grants CA257195, CA254104 and CA154947. T.U.M. and the clinical trial presented in Fig. 4 were partially supported by the Feldman Foundation. N.M.L. was supported by the Cancer Research Institute/Bristol Myers Squibb Irvington Postdoctoral Research Fellowship to Promote Racial Diversity (award no. CRI3931). S.H. was supported by the National Cancer Institute predoctoral-to-postdoctoral fellowship K00 CA223043. R.M. was supported by the 2021 AACR-AstraZeneca Immuno-oncology Research Fellowship, Grant Number 21-40-12-MATT. O.C.O. was supported by the Cancer Research Institute Irvington Postdoctoral Research Fellowship (award no. CRI3617). B.D.B. was partially supported by NIH grant U01CA282114. S.G. was partially supported by NIH grants CA224319, DK124165, CA263705 and CA196521.

Author contributions N.M.L., M.M. and T.U.M. conceptualized and obtained funding for the project. N.M.L., M.M. and T.U.M. designed experiments. N.M.L., S.H., M.D.P., J.L.B., B.B.M., L.T., I.R.-T, M. Belabed, R.M., A.M.R., R.Z., O.C.O. and E.N. performed experiments. N.M.L., M.D.P., S.H. and P.H. analysed experiments. D.B.D., N.C.R., J.E.G., R.V., N.H. and T.U.M. provided clinical care to patients in the clinical trial. C.H., T.C. and N.V. managed clinical specimens. M. Buckup, I.F., V.R., S.G., E.G.-K., K.M., H.K., F.G., Z.L., E.P., S.K.-S., B.D.B., F.R.H. and B.S.K. provided intellectual input, essential reagents and computational tools. N.M.L. wrote the manuscript. M.M. and T.U.M. edited the manuscript. All authors provided feedback on the manuscript draft.

Competing interests M.M. and T.U.M. have submitted a patent related to the clinical trial described in this study. M.M. serves on the scientific advisory board and holds stock from Compugen Inc., Myeloid Therapeutics Inc., Morphic Therapeutic Inc., Asher Bio Inc., Dren Bio Inc., Oncoresponse Inc., Owkin Inc., Larkspur Inc. and DEM BIO, Inc. M.M. serves on the scientific advisory board of Innate Pharma Inc., OSE Inc. and Genenta Inc. M.M. receives funding for contracted research from Regeneron Inc. and Boerhinger Ingelheim Inc. T.U.M. has served on Advisory and/or Data Safety Monitoring Boards for Rockefeller University, Regeneron Pharmaceuticals, Abbvie, Bristol Myers Squibb, Boehringer Ingelheim, Atara, AstraZeneca, Genentech, Celldex, Chimeric, Glenmark, Simcere, Surface, G1 Therapeutics, NGMbio, DBV Technologies, Arcus and Astellas, and has research grants from Regeneron, Bristol-Myers Squibb, Merck and Boehringer Ingelheim. B.S.K. is a consultant for Regeneron and Sanofi. D.B.D. sits on the advisory boards of Astrazeneca, Mirati Therapeutics, Summit Therapeutics, G1 Therapeutics and Sanofi, and is a consultant for Sonata Therapeutics. S.G. reports other research funding from Boehringer Ingelheim, Bristol-Myers Squibb, Celgene, Genentech, Regeneron and Takeda not related to this study.

Additional information
Supplementary information The online version contains supplementary material available at https://doi.org/10.1038/s41586-023-06797-9.

Correspondence and requests for materials should be addressed to Miriam Merad.

Peer review information *Nature* thanks Benjamin Izar, Elvira Mass and the other, anonymous, reviewer(s) for their contribution to the peer review of this work.

Reprints and permissions information is available at http://www.nature.com/reprints.

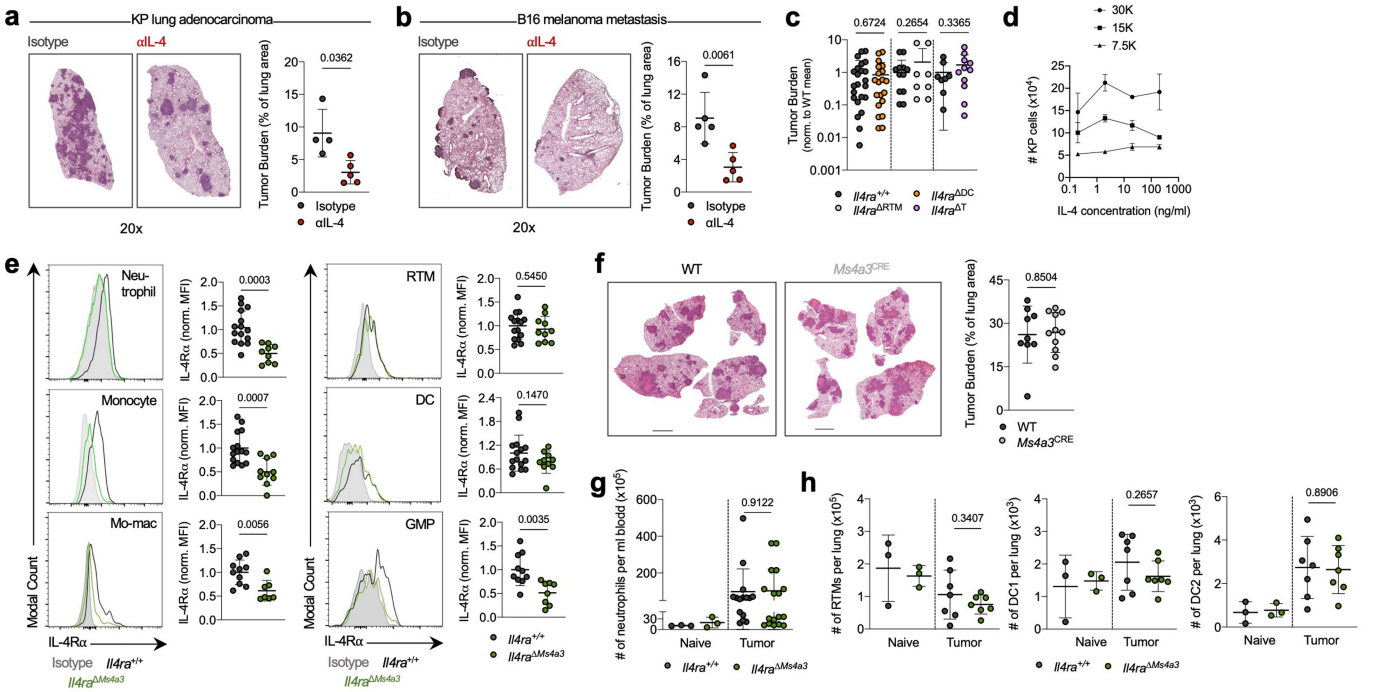

Extended Data Fig. 1 | A role for myeloid IL-4Rα expression in NSCLC development. (a-b) Tumor burden in KP-lung tumor (a) and B16 melanoma metastasis (b) bearing mice treated with isotype or αIL-4 antibodies. Images at 20X. $n = 4$ mice per group in panel a; $n = 5$ mice per group in panel b. Representative of two independent experiments. (c) KP lung tumor burden in $Il4ra^{\Delta DC}$, $Il4ra^{\Delta RTM}$, and $Il4ra^{\Delta T}$ mice normalized to WT littermate controls (n = 8-24 mice per group). $n = 24, 22, 16, 9, 8, 11$ mice per group. Pooled from three independent experiments. (d) Number of viable KP cells at indicated seeding values after 5 days of culture in complete media with indicated concentrations of IL-4. Two technical replicates per timepoint. Representative of two independent experiments. (e) IL-4Rα expression in indicated myeloid populations of tumor-bearing $Il4ra^{+/+}$ and $Il4ra^{\Delta Ms4a3}$ mice, normalized to mean MFI of $Il4ra^{+/+}$ group. $n = 15$ $Il4ra^{+/+}$ mice and 9 $Il4ra^{\Delta Ms4a3}$ mice for neutrophils; 15 $Il4ra^{+/+}$ mice and 10 $Il4ra^{\Delta Ms4a3}$ mice for monocytes, RTMs, and DCs; 10 $Il4ra^{+/+}$ mice and 7 $Il4ra^{\Delta Ms4a3}$ mice for mo-macs, and 10 $Il4ra^{+/+}$ mice and 8 $Il4ra^{\Delta Ms4a3}$ mice for GMPs. Pooled from three independent experiments. (f) KP tumor burden in *Ms4a3-Cre* heterozygous mice bearing no floxed allele ($n = 11$) compared to age-matched WT controls ($n = 9$). Scale bar=2 mm. One experiment. (g) Number of circulating blood neutrophils in naïve and KP tumor-bearing $Il4ra^{+/+}$ and $Il4ra^{\Delta Ms4a3}$ mice. $n = 3, 3, 15, 17$ mice per group. Pooled from 3 independent experiments. (h) Number of lung myeloid populations in naïve and KP tumor-bearing $Il4ra^{+/+}$ and $Il4ra^{\Delta Ms4a3}$ mice. $n = 3, 3, 7, 7$ mice per group. Representative of two independent experiments. Unpaired two-tailed Student's *t*-test for all statistical analyses shown. Data are mean ± s.d.

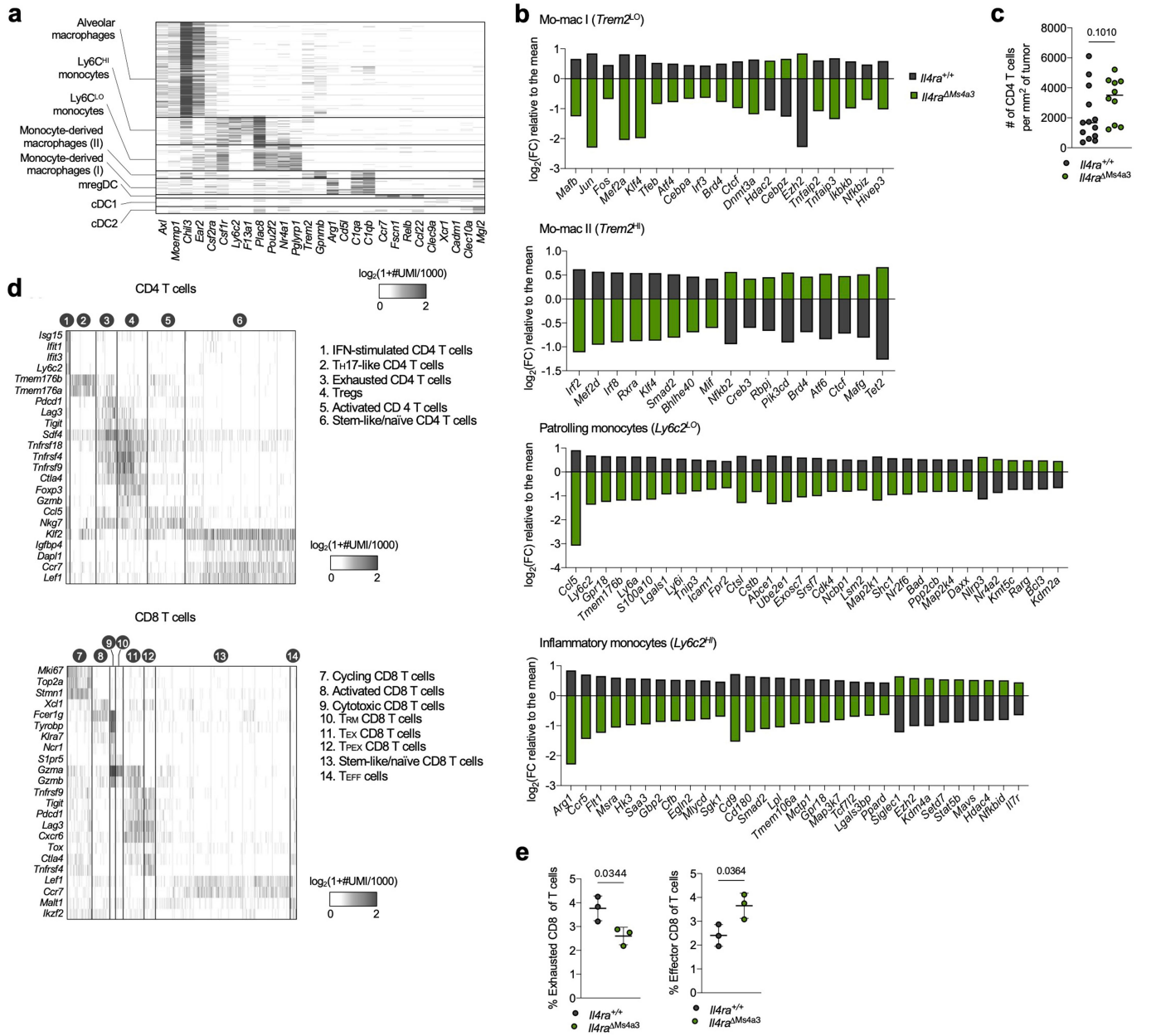

Extended Data Fig. 2 | Transcriptional and histological analyses of lung tumors in *Il4ra*$^{+/+}$ and *Il4ra*$^{\Delta Ms4a3}$ mice. (a) Heatmap showing myeloid scRNA-seq clusters (y axis) along with cluster-defining genes (x axis). (b) Gene expression in indicated lung immune clusters of tumor-bearing *Il4ra*$^{+/+}$ and *Il4ra*$^{\Delta Ms4a3}$ mice ($n = 3$ mice per group). One experiment. (c) Average number of CD4 T cells per mm^2 of tumor in KP lesions of *Il4ra*$^{+/+}$ ($n = 13$) and *Il4ra*$^{\Delta Ms4a3}$ ($n = 10$) mice. Representative of three independent experiments. (d) Heatmap showing scRNA-seq clusters from sorted T cells (left) and fine-clustered CD4 (middle) and CD8 (right) T cells (y axis) along with cluster-defining genes (x axis). One experiment. (e) Proportion of the "Exhausted CD8" and "Effector CD8" clusters from panel d among all lung T cells in *Il4ra*$^{+/+}$ and *Il4ra*$^{\Delta Ms4a3}$ mice ($n = 3$ mice per group). One experiment. Data are mean (b), median (c), or mean ± s.d (e). Mann-Whitney test (c) or unpaired two-tailed Student's *t*-test (e).

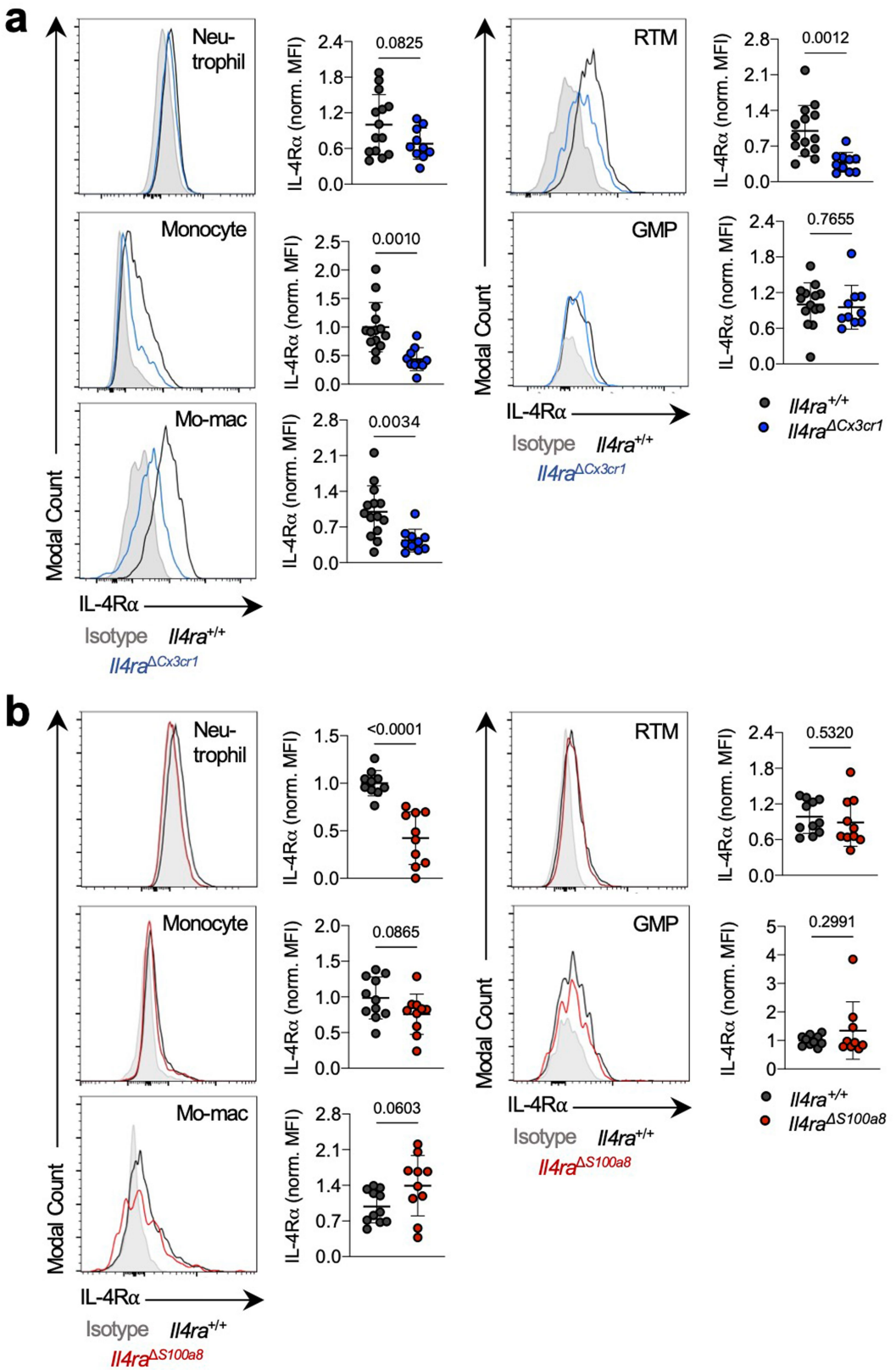

Extended Data Fig. 3 | IL-4Rα expression in myeloid populations of tumor-bearing *Il4ra*$^{\Delta Cx3cr1}$ and *Il4ra*$^{\Delta S100a8}$ mice compared to littermate controls. Representative flow cytometry histograms showing IL-4Rα protein expression in indicated immune populations from tumor-bearing *Il4ra*$^{\Delta Cx3cr1}$ and *Il4ra*$^{\Delta S100a8}$ mice along with WT littermate controls, normalized to mean MFI of WT group. $n = 14$ *Il4ra*$^{+/+}$ and 10 *Il4ra*$^{\Delta Cx3cr1}$ mice; 10 *Il4ra*$^{+/+}$ and 10 *Il4ra*$^{\Delta S100a8}$ mice for neutrophils; 11 *Il4ra*$^{+/+}$ and 10 *Il4ra*$^{\Delta S100a8}$ mice for monocytes; mo-macs, and RTMs; 10 *Il4ra*$^{+/+}$ and 9 *Il4ra*$^{\Delta S100a8}$ mice for GMPs. Pooled from three independent experiments. Grey histogram = Isotype control. Unpaired two-tailed Student's *t*-test. Data are mean ± s.d.

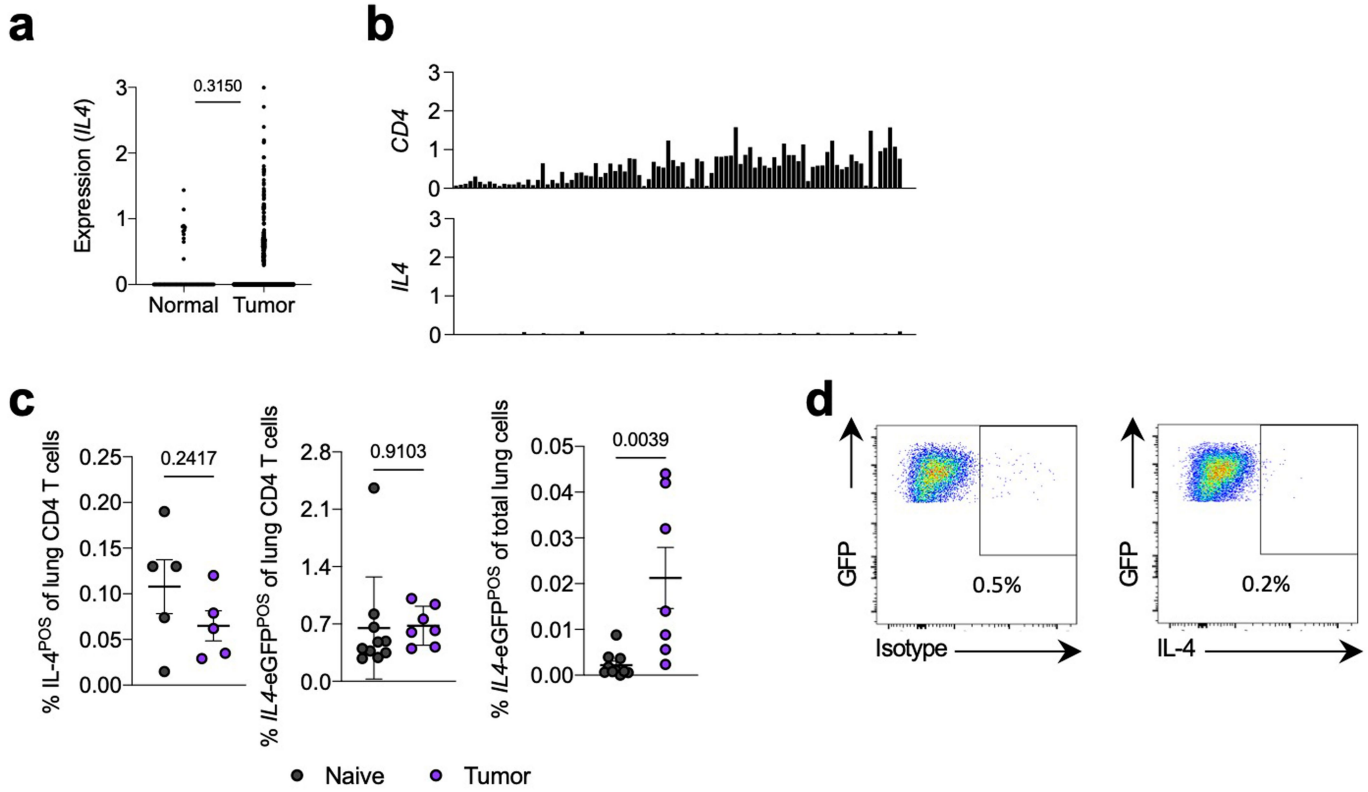

Extended Data Fig. 4 | No evidence for Th2-biased immune microenvironment in NSCLC. (a) Expression of *IL4* in matched NSCLC tumors and adjacent normal tissue from TCGA database. (b) Expression of indicated genes (y axis) across T cell clusters (x axis) from Leader et al human NSCLC scRNA-seq dataset. (c) IL-4 production after PMA/I stimulation (left) and *IL4*-eGFP expression in CD4 T cells (middle) and total live cells (right) from lungs of naïve and tumor-bearing mice. $n = 5$ mice per group for IL-4^{POS} lung CD4 T cells, 10 naïve and 10 tumor-bearing mice for *IL4*-eGFP^{POS} CD4 T cells and total *IL4*-eGFP^{POS} cells. Representative of two independent experiments. (d) IL-4 production by lung-seeding KP cells in vivo after PMA/I stimulation. One experiment. Unpaired two-tailed Student's *t*-test. Data are mean ± s.d.

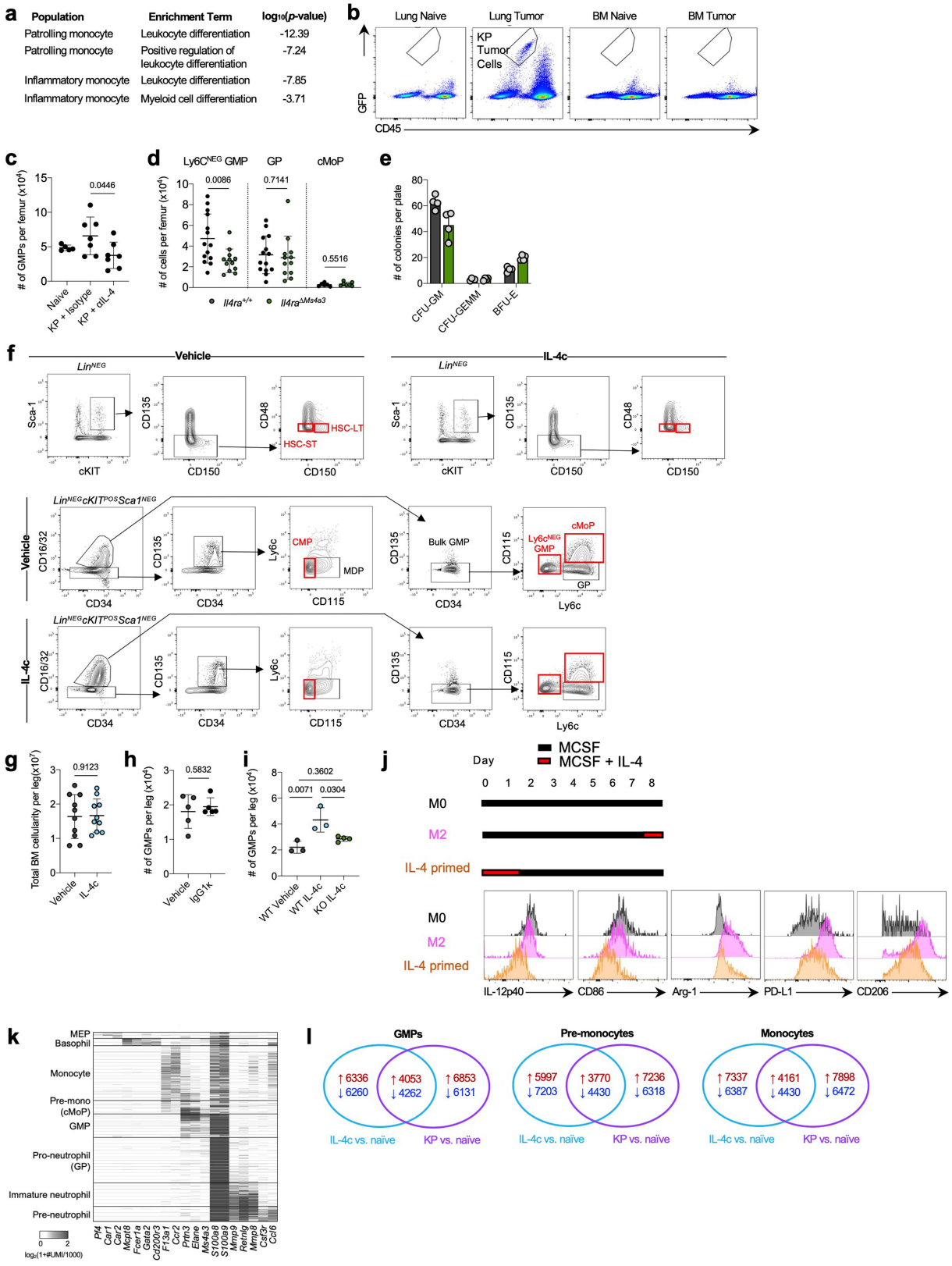

Extended Data Fig. 5 | See next page for caption.

Extended Data Fig. 5 | IL-4 controls myelopoiesis. (a) Top pathways enriched among DEGs from indicated lung monocyte populations in tumor-bearing *Il4ra*$^{+/+}$ and *Il4ra*$^{\Delta Ms4a3}$ mice. (b) Flow cytometry plots showing CD45^{NEG}GFP^{POS} cells in lung and BM of mice bearing GFP-expressing KP tumors. (c) Number of GMPs per femur of naïve mice or KP tumor-bearing mice treated with isotype or αIL-4 antibodies. n = 5, 7, 7 mice per group. Representative of two independent experiments. (d) Number of Ly6c^{NEG} GMP, GP, and cMoP progenitors in BM of KP tumor-bearing *Il4ra*$^{+/+}$ and *Il4ra*$^{\Delta Ms4a3}$ mice. n = 14 *Il4ra*$^{+/+}$ and 12 *Il4ra*$^{\Delta Ms4a3}$ mice for Ly6c^{NEG} GMPs and GPs and 6 *Il4ra*$^{+/+}$ and 7 *Il4ra*$^{\Delta Ms4a3}$ mice for cMoPs. Pooled from two independent experiments. (e) Methocult differentiation assay of *Il4ra*$^{+/+}$ and *Il4ra*$^{\Delta Ms4a3}$ BM. n = 4 technical replicates per condition. Representative of two independent experiments. (f) Representative gating strategy for BM progenitor populations in vehicle and IL-4c treated mice. (g) Total BM cellularity from legs of WT mice treated with vehicle or IL-4c (n = 10 mice per group). Pooled from two independent experiments. (h) Number of GMPs per leg of mice treated with vehicle or IgG1κ antibodies. n = 5 mice per group. One experiment (i) Number of GMP per leg of *Il4ra*$^{+/+}$ (WT) or *Il4ra*$^{\Delta Ms4a3}$ (KO) mice treated with vehicle or IL-4c. n = 3, 3, 4 mice per group. One experiment. (j) Expression of macrophage polarization markers in BMDMs differentiated under indicated conditions. Representative of two independent experiments. (k) scRNA-seq of BM myeloid cells and myeloid progenitors from naïve, IL-4c treated, and KP tumor-bearing mice. Heatmap shows indicated clusters (y axis) and cluster-defining genes (x axis). (l) Total number of genes up or downregulated in each condition relative to naïve in indicated BM scRNA-seq clusters. One experiment. Fisher's Exact Test (a), Unpaired two-tailed Student's t-test (c,d,g,h), or One-way ANOVA with *post hoc* Tukey's test (i). Data are mean ± s.d. Lin = CD3e, B220, Ter-119, CD11b, Ly6g, NK1.1.

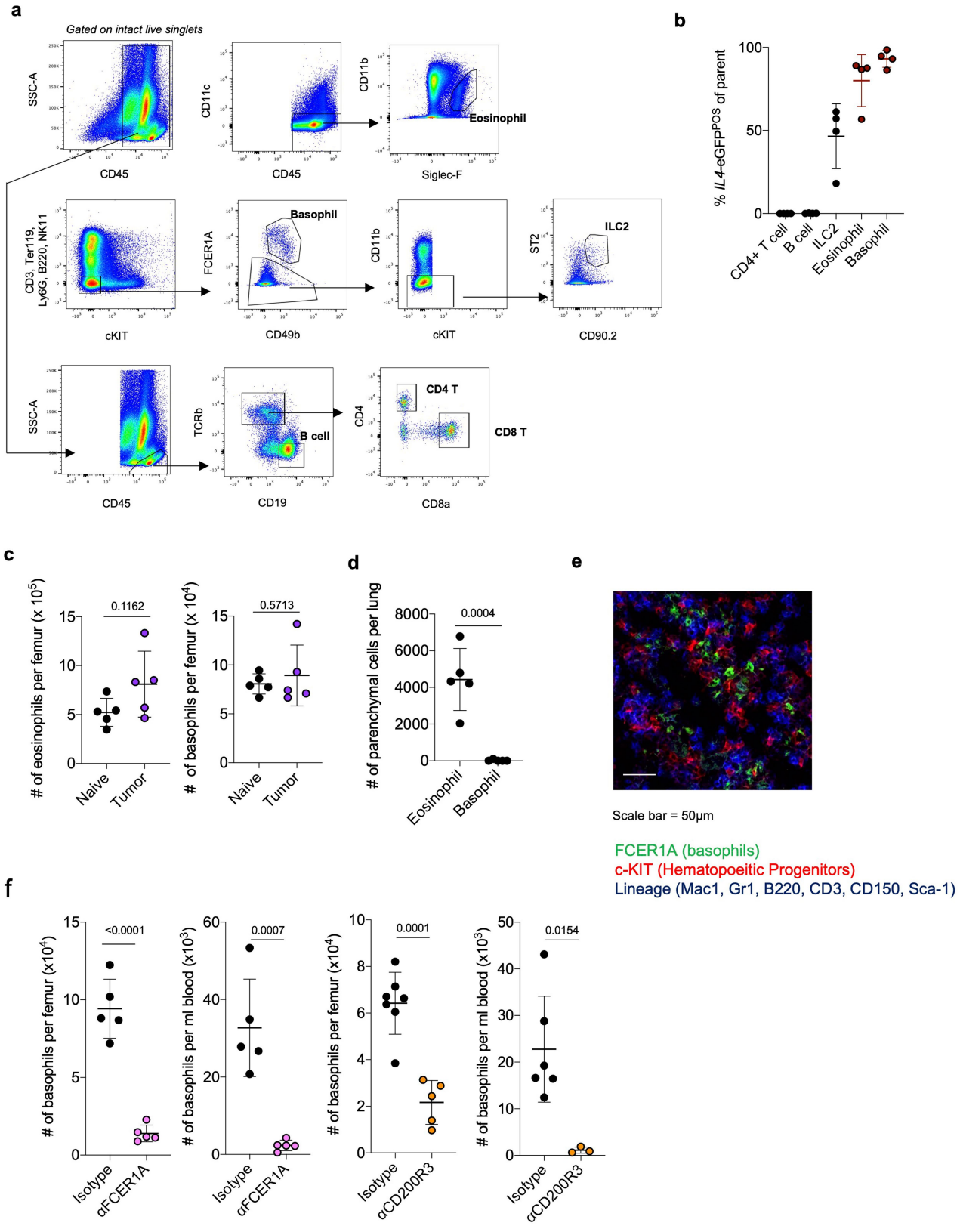

Extended Data Fig. 6 | Dynamics of Type 2 granulocytes in BM. (a) Flow cytometry strategy for BM populations analyzed in Fig. 3a. (b) Percentage of *IL4*-eGFP^{POS} cells among indicated BM populations in WT KP tumor-bearing mice. $n = 5$ mice. Representative of two independent experiments. (c) Number of BM eosinophils and basophils in naïve and tumor-bearing WT mice. $n = 5$ mice per group. Representative of two independent experiments. (d) Number of CD45-IV negative eosinophils and basophils in lungs of tumor-bearing WT mice. $n = 5$ mice per group. Representative of two independent experiments. (e) Representative microscopy of BM of tumor-bearing mice showing colocalization of basophils (green) with hematopoietic progenitors (red) (representative of 3 mice). (f) Basophil depletion efficiency in indicated organs after using αFCER1A (left) or αCD200R3 (right) depletion strategies $n = 5$ isotype and 5 αFCER1A-treated mice; 7 isotype and 5 αCD200R3-treated mice for BM; 6 isotype and 3 αCD200R3-treated mice for blood. Unpaired two-tailed Student's *t*-test. Data are mean ± s.d.

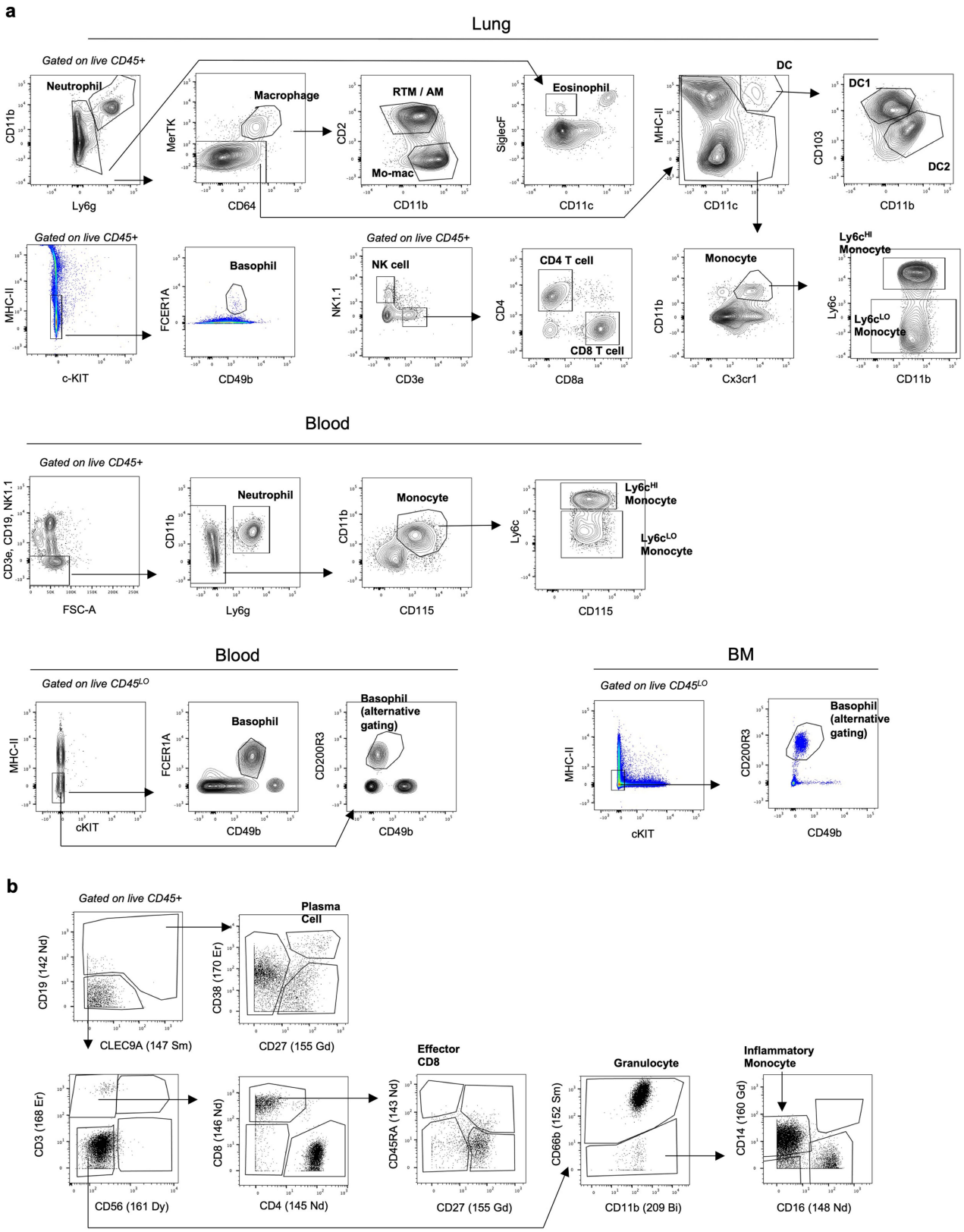

Extended Data Fig. 7 | Gating Strategies. (a) Flow cytometry gating strategy for indicated mouse immune populations. Note "basophil alternative gating" using CD200R3 was used in experiments where mice were treated with αFCER1A antibodies. (b) CyTOF gating strategy for human whole blood.

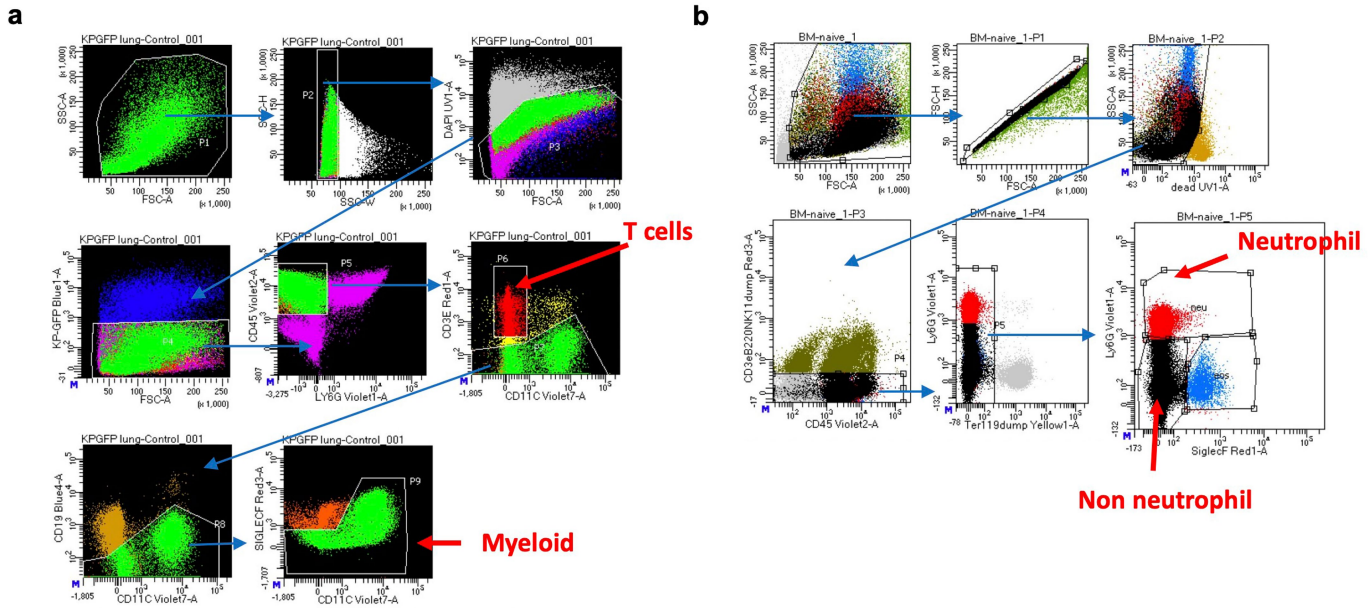

Extended Data Fig. 8 | Sorting Strategies. (a-b) Sorting strategies for scRNA-seq experiments presented in Fig. 1(a) and Fig. 2(b).

nature portfolio

Corresponding author(s): Miriam Merad

Last updated by author(s): Oct 13, 2023

Reporting Summary

Nature Portfolio wishes to improve the reproducibility of the work that we publish. This form provides structure for consistency and transparency in reporting. For further information on Nature Portfolio policies, see our Editorial Policies and the Editorial Policy Checklist.

Statistics

For all statistical analyses, confirm that the following items are present in the figure legend, table legend, main text, or Methods section.

n/a	Confirmed	
☐	☒	The exact sample size (*n*) for each experimental group/condition, given as a discrete number and unit of measurement
☐	☒	A statement on whether measurements were taken from distinct samples or whether the same sample was measured repeatedly
☐	☒	The statistical test(s) used AND whether they are one- or two-sided *Only common tests should be described solely by name; describe more complex techniques in the Methods section.*
☐	☒	A description of all covariates tested
☐	☒	A description of any assumptions or corrections, such as tests of normality and adjustment for multiple comparisons
☐	☒	A full description of the statistical parameters including central tendency (e.g. means) or other basic estimates (e.g. regression coefficient) AND variation (e.g. standard deviation) or associated estimates of uncertainty (e.g. confidence intervals)
☐	☒	For null hypothesis testing, the test statistic (e.g. *F*, *t*, *r*) with confidence intervals, effect sizes, degrees of freedom and *P* value noted *Give P values as exact values whenever suitable.*
☒	☐	For Bayesian analysis, information on the choice of priors and Markov chain Monte Carlo settings
☒	☐	For hierarchical and complex designs, identification of the appropriate level for tests and full reporting of outcomes
☐	☒	Estimates of effect sizes (e.g. Cohen's *d*, Pearson's *r*), indicating how they were calculated

Our web collection on statistics for biologists contains articles on many of the points above.

Software and code

Policy information about availability of computer code

Data collection	Data from flow cytometry were collected on a BD LSRFortessa Analyzer using BD FACSDiva v8.0.2 software.
Data analysis	Flow cytometry data were analyzed using Flow Jo version 10. Statistics were performed on Graphpad Prism 8. For RNAseq, Gene set enrichment analysis was performed using the Enrichr database. Other R packages used for single-cell (and bulk RNA) analysis of newly generated and published datasets include: shiny v.1.7.1; ShinyTree v.0.2.7, heatmaply v.1.3.0; plotly v.4.10.0; ggvis v.0.4.7; gpplot2 v.3.3.5; dplyr v.1.0.7; Matrix v.0.9.8; seriation v.1.3.5

For manuscripts utilizing custom algorithms or software that are central to the research but not yet described in published literature, software must be made available to editors and reviewers. We strongly encourage code deposition in a community repository (e.g. GitHub). See the Nature Portfolio guidelines for submitting code & software for further information.

Data

Policy information about availability of data

All manuscripts must include a data availability statement. This statement should provide the following information, where applicable:

- Accession codes, unique identifiers, or web links for publicly available datasets
- A description of any restrictions on data availability
- For clinical datasets or third party data, please ensure that the statement adheres to our policy

Code for generating specific figures will be provided by the corresponding author upon reasonable request. Raw RNA-seq data has been deposited in the Gene

Expression Omnibus (GEO) under accession code GSE245236.
CT images of patients participating in the clinical trial can be downloaded via Amazon Web Services at the following link: https://himc-project-data.s3.amazonaws.com/lamarche_2023/lamarche_image_data.tar.gz?AWSAccessKeyId=AKIAV3HQ5KORNL3V6W43&Signature=N32aM3ouC5FwYvbMvA7eJJd3V4k%3D&Expires=1698691876

Human research participants

Policy information about studies involving human research participants and Sex and Gender in Research.

Reporting on sex and gender	Biological sex was reported for all patients involved in the clinical trial. Biological sex was equally distributed in patient and control groups analyzed in Fig. 3k.
Population characteristics	Relevant characteristics from all patients involved in the clinical trial can be found in Supplementary Table 5.
Recruitment	Patients were referred to this trial by treating physicians from the Mount Sinai Center for Thoracic Oncology. There were no potential self-selection biases.
Ethics oversight	All human studies were performed with the oversight and approval of the Institutional Review Board of the Icahn School of Medicine at Mount Sinai

Note that full information on the approval of the study protocol must also be provided in the manuscript.

Field-specific reporting

Please select the one below that is the best fit for your research. If you are not sure, read the appropriate sections before making your selection.

☒ Life sciences ☐ Behavioural & social sciences ☐ Ecological, evolutionary & environmental sciences

For a reference copy of the document with all sections, see nature.com/documents/nr-reporting-summary-flat.pdf

Life sciences study design

All studies must disclose on these points even when the disclosure is negative.

Sample size	No statistical methods were used to determine sample size, and sample size was determined based on availability of mice. Sample size was validated as adequate based on reproducibility between independent experiments.
Data exclusions	In scRNA-seq data, cells were excluded based on commonly-used, pre-established criteria (low number of detectable transcripts, erythrocyte transcriptional content, and high mitochondrial transcriptional content. Additional information on cell filtering is available in Leader et al 2021 Cancer Cell. A Grubbs test was used to remove one statistical outlier in Figures 1c, 1f, and 4a.
Replication	All experiments were replicable and performed at least two times unless otherwise indicated.
Randomization	Mice were randomly assigned to treatment or control groups. Human studies profiled NSCLC patients and healthy controls; therefore, no randomization was required. For the clinical trial described in Figure 4, all patients received dupilumab treatment, so there was no need for randomization.
Blinding	Due to the objective manner of analysis, researchers were not blinded in these studies.

Reporting for specific materials, systems and methods

We require information from authors about some types of materials, experimental systems and methods used in many studies. Here, indicate whether each material, system or method listed is relevant to your study. If you are not sure if a list item applies to your research, read the appropriate section before selecting a response.

Materials & experimental systems

n/a	Involved in the study
☐	☒ Antibodies
☐	☒ Eukaryotic cell lines
☒	☐ Palaeontology and archaeology
☐	☒ Animals and other organisms
☐	☒ Clinical data
☒	☐ Dual use research of concern

Methods

n/a	Involved in the study
☒	☐ ChIP-seq
☐	☒ Flow cytometry
☒	☐ MRI-based neuroimaging

Antibodies

Antibodies used

Mouse Flow Cytometry:
CD45 (clone 30-F11, Biolegend, ref# 103138, 1:100), IL-4Rα (clone I015F8, Biolegend, ref# 144805, 1:100), IL-4 (clone 11B11, ThermoFisher, ref# 17-7041-81, 12-7041-82, 1:100), IL-12p40 (clone C17.8, ThermoFisher, ref# 505211, 1:100), CD103 (clone 2E7, Biolegend, ref# 13-1031-82, 1:100), CD11b (clone M1/70, Biolegend ref# 101230, ThermoFisher ref# 47-0112-82, 1:200), CD11c (clone N418, Biolegend, ref# 117336, 1:400), CD127 (clone A7R34, Biolegend, ref# 135019, 1:100), CD4 (clone RM4-5, Biolegend, ref# 100545, 1:200), CD8a (clone 53-6.7, Biolegend, ref# 100714, 1:200), CD3 (clone 17A2, ThermoFisher, ref# 47-0032-82, 1:200), Cx3cr1 (clone SA011F11, Biolegend, ref# 149023, 1:200), Ly6g (clone 1A8, ref# 127624, Biolegend, 1:200), Ly6c (clone HK1.4, Biolegend ref# 128035, Thermofisher ref# 17-5932-82, 1:400), TCRb (clone H57-597, Biolegend, ref# 109228, 1:400). Siglec F (clone E50-2440, BD Pharmingen, ref# 562680, 565527, 1:100), MHC II I-A/I-E (clone M5/114.15.2, Biolegend, ref# 107643, 1:400), CD115 (clone AFS98, eBioscience, ref# 17-1152-82, 13-1152-85, 1:100), CD2 (clone RM2-4, Biolegend, ref# 100114, 1:200), MerTK (clone DS5MMER, eBioscience, ref# 12-5751-82, 1:100), CD64 (clone X54-5/7.1, ThermoFisher ref# 17-0641-82, Biolegend ref# 139318, 1:100), CD16/CD32 (clone 93, ThermoFisher, ref# 56-0161-82, 1:300), CD34 (clone HM34, Biolegend, ref #128612; clone RAM34, ThermoFisher, ref# 48-0341-82, 1:100), c-kit (clone 2B8, Biolegend ref# 553353, ThermoFisher ref# 25-1171-82, 1:100), ST2 (clone RMST2-2, ThermoFisher, ref# 46-9335-82, 1:100), Sca-1 (clone D7, ThermoFisher, ref# 25-0981-81, Biolegend ref# 108126, 1:100), CD150 (clone mShad150, ThermoFisher, ref# 17-1502-80, 1:100), CD48 (clone HM48-1, ThermoFisher, ref# 46-0481-80, 1:100), CD135 (clone A2F10, Biolegend, ref# 135306, 1:50), NK1.1 (clone PK136, Biolegend ref# 108724, ThermoFisher ref# 45-5941-82, 1:100), CD19 (clone eBio1D3, ThermoFisher, ref# 48-0193-82, 1:200), Ter-119 (clone Ter-119, ThermoFisher, ref# 47-5921-82, 1:200), B220 (clone RAB-632, ThermoFisher, ref# 47-0452-82, 1:200), FCER1A (clone MAR-1, Biolegend, ref# 134308, 1:100), CD49b (clone DX5, eBioscience, ref# 48-5971-82, 1:100), Arg-1 (clone A1exF5, eBioscience, ref# 53-3697-82, 1:100), F4/80 (clone BM8, ThermoFisher, ref# 48-4801-82, 1:200), CD200R3 (Clone Ba13, Biolegend, ref# 142205, 1:100), CD86 (clone GL-1, Biolegend, ref# 105006, 1:100), pSTAT6 (Tyr641) (clone CHI2S4, eBioscience, ref# 17-9013-42, 1:100), CD90.2 (clone 30-H12, ThermoFisher, ref# 25-0902-81, 1:200), CD45.2 (clone 104, Biolegend ref# 109830, ThermoFisher ref# 47-0454-82, 1:200), CD45.1 (clone A20, Biolegend, ref# 110741, 1:200), PD-L1 (clone MIH5, ThermoFisher, ref# 12-5982-82, 1:200), CD206 (clone C068C2, Biolegend, ref# 141703, 1:200).

Human CyTOF (note- all antibodies used at 1:100)
CD45 (clone HI30, Fluidigm, ref# 3089003B), HLA-ABC (cloneW6/32, Biolegend, ref# 311402), CD11c (clone REA618, Miltenyi, ref# 130-122-296), CD33 (clone WM53, Biolegend, ref# 303410), CD19 (clone REA675, Miltenyi, ref# 130-122-301), CD45RA (clone REA562, Miltenyi, ref# 130-122-292), CD141 (clone Phx-01, Biolegend, ref# 902101), CD4 (clone, REA623 Miltenyi, ref# 130-122-283), CD8 (clone REA734, Miltenyi, ref# 130-122-281), CLEC9A (clone 8F9, Miltenyi, ref# 130-122-306), CD16 (clone REA423, Miltenyi, ref# 130-108-027), FceRIa (clone AER-37, Biolegend, ref# 334602), CD1c (clone REA694, Miltenyi, ref# 130-122-298), CD123 (clone REA918, Miltenyi, ref# 130-122-297), CD66B (clone REA306, Miltenyi, ref# 130-108-019), CD83 (clone HB15e, Biolegend, ref# 130-108-019), CD163 (clone GHI/61, Fluidigm, ref# 3154007B), CD27 (clone REA499, Miltenyi, ref# 130-122-295), CD86 (clone IT2.2, Fluidigm, ref# 3156008B), PD-L1 (clone 29E.2A3, Fluidigm, ref# 3159029B), CD14 (clone REA599, Miltenyi, ref# 130-122-290), CD56 (clone REA196, Miltenyi, ref# 130-108-016), CD64 (clone 10.1, Biolegend, ref# 305002), CD172a/b (clone SE5A5, Fluidigm, ref# 3163017B), CD40 (clone HB14, Biolegend, ref# 334302), CD169 (clone 7-239, Biolegend, ref# 346002), CD117 (clone 104D2, Biolegend, ref# 313202), CD3 (clone REA613, Miltenyi, ref# 130-122-282), CD38 (clone REA671, Miltenyi, ref# 130-122-288), CD207 (clone 1.00E+03, Biolegend, ref# 352202), CD206 (clone 15-2, Biolegend, ref# 321102), CD226 (clone 11A8, Biolegend, ref# 338302), HLADR (clone REA805, Miltenyi, ref# 130-122-299), Axl (clone 108724, R&DSystems, ref# MAB154), CD209 (clone 9E9A8, Biolegend, ref# 330102), CD11b (clone ICRF44, Fluidigm, ref# 3209003B).

Human Immunohistochemistry
CD8a (clone C8/144B, Dako, ref# M7103, 1:100), DC-LAMP (clone DX0191P, Novus Biological, ref# DDX0191P, 1:80), CD20 (clone L26, Dako, ref# M0755, 1:250)

Mouse Immunohistochemistry
CD3e (Polyclonal, ThermoFisher, ref# PA5-32318, 1:100), CD8a (clone FSM15, eBioscience, ref# 14-0818-82, 1:100), Gzmb (Polyclonal, R&D Systems, ref# AF1865, 1:25), NCR1 (clone mNCR1.05, Abcam, ref# ab283505, 1:250).

Mouse Immunofluorescence
For basophil staining, anti-FCER1A (MAR-1, ThermoFisher 14-5898-82) was used at 1:200 dilution and followed by goat anti-Armenian hamster IgG conjugated to A488 (Jackson ImmunoResearch, 127-545-160) at 1:500 dilution. For hematopoietic progenitor staining, anti-CD117 (ACK2, Biolegend 135102) was used at 1:25 dilution and followed by goat anti-rat Cy3 (Jackson Immunoresearch, 112-165-167) at 1:100 dilution. For lineage staining, a combination of anti-Mac1 (M1/70, Biolegend 101218), anti-Gr1 (RB6-8C5, Biolegend 108418), anti-B220 (RA3-6B2, Biolegend 103226), anti-CD3 (17A2, Biolegend 100209), anti-CD150 (TC15-12F12.2, Biolegend 115918), anti-Sca1 (D7, Biolegend 108118) all directly conjugated to A647 and at 1:100 dilution was used.

In vivo (all antibodies injected in 100µl of sterile saline)
anti-IL4 (clone 11B11, BioXcell, ref # BE0045, 25µg), anti-FCER1A (clone MAR-1, ThermoFisher, ref# 14-5898-85, 10µg), anti-CD200R3

(clone Ba103, Hajime Karasuyama lab, 50µg), anti-PD-L1 (clone 10F.9G2, BioXcell, ref# BE0101, 200µg), Rat IgG1 isotype control (clone HRPN, BioXcell, ref# BE0088, 25µg), Armenian hamster IgG isotype control (clone eBio299Arm, ThermoFisher, ref# 16-4888-85, 10µg), Rat IgG2b isotype antibody (clone RTK4530, Biolegend, ref# 400602, 50µg), Rat IgG2b isotype antibody (clone LTF-2, BioXcell, ref# BE0090, 200µg).

Validation

Mouse Flow cytometry
CD45: Flow cytometry of mouse splenocytes (website).
IL-4Rα: Flow cytometry of mouse splenocytes (website).
IL-4: Flow cytometry of Th2-polarized mouse splenocytes (website).
IL-12p40: Flow cytometry of mouse splenocytes (website).
CD103: Flow cytometry of mouse splenocytes (website).
CD11b: Flow cytometry of mouse splenocytes (website).
CD11c: Flow cytometry of mouse splenocytes (website).
CD127: Flow cytometry of mouse splenocytes (website).
CD4: Flow cytometry of mouse splenocytes (website).
CD8a: Flow cytometry of mouse splenocytes (website).
CD3: Flow cytometry of mouse splenocytes (website).
Cx3cr1: Flow cytometry of mouse splenocytes (website).
Ly6g: Flow cytometry of mouse splenocytes (website).
Ly6c: Flow cytometry of mouse splenocytes (website).
Tcrb: Flow cytometry of mouse splenocytes (website).
Siglec F: Flow cytometry of mouse bone marrow (website).
MHC II I-A/I-E: Flow cytometry of mouse splenocytes (website).
CD115: Flow cytometry of thioglycolate-induced peritoneal exudate cells (website).
CD2: Flow cytometry of mouse splenocytes (website).
MerTK: Flow cytometry of peritoneal exudate cells (website).
CD64: Flow cytometry of mouse bone marrow (website).
CD16/CD32: Flow cytometry of mouse splenocytes (website).
CD34: Flow cytometry of mouse fibroblast NIH/3T3 cells (website).
c-kit: Flow cytometry of mouse bone marrow (website).
ST2: Flow cytometry of mouse bone marrow-derived mast cells (website).
Sca-1: Flow cytometry of mouse bone marrow (website).
CD150: Flow cytometry of mouse splenocytes (website).
CD48: Flow cytometry of mouse splenocytes (website).
CD135: Flow cytometry of mouse bone marrow (website).
NK1.1: Flow cytometry of mouse splenocytes (website).
CD19: Flow cytometry of mouse splenocytes (website).
Ter-119: Flow cytometry of mouse bone marrow (website).
FCER1A: Flow cytometry of MC/9 cell line (website).
CD49b: Flow cytometry of mouse splenocytes (website).
Arg-1: Flow cytometry of whole blood (website).
F4/80: Flow cytometry of peritoneal exudate cells (website).
CD200R3: Flow cytometry of MC/9 cells (website).
CD86: Flow cytometry of LPS-stimulated mouse splenocytes (website).
pSTAT6: Flow cytometry of IL-4 stimulated Th2 polarized CD4 cells (website).
CD90.2: Flow cytometry of mouse thymocytes (website).
CD45.2: Flow cytometry of mouse splenocytes (website)
CD45.1: Flow cytometry of mouse splenocytes (website). .
PD-L1: Flow cytometry of mouse splenocytes (website).
CD206: Flow cytometry of peritoneal exudate cells.

Human CyToF antibodies
CD45: CyTOF of human PBMCs (website)
HLA-ABC: Flow cytometry of human PBMCs (website)
CD11c: Flow cytometry of human PBMCs (website.)
CD33: Flow cytometry of human PBMCs (website).
CD19: Flow cytometry of human PBMCs (website).
CD45RA: Flow cytometry of human PBMCs (website).
CD141: IHC staining of human placenta (website).
CD4: Flow cytometry of human PBMCs (website).
CD8: Flow cytometry of human PBMCs (website).
CLEC9A: Flow cytometry of human PBMCs (website).
CD16: Flow cytometry of human PBMCs (website).
FCER1A: Flow cytometry of human PBMCs (website).
CD1c: Flow cytometry of human PBMCs (website).
CD123: Flow cytometry of human PBMCs (website).
CD66b: Flow cytometry of human peripheral blood cells (website).
CD83: Flow cytometry of human monocyte-derived dendritic cells (website).
CD163: Flow cytometry of human PBMCs (website).
CD27: Flow cytometry of human PBMCs (website).
CD86: Flow cytometry of human PBMCs (website).
PD-L1: Flow cytometry of human PBMCs (website).
CD14: Flow cytometry of human PBMCs (website).
CD56: Flow cytometry of human PBMCs (website).

CD64: Flow cytometry of human peripheral blood monocytes (website).
CD172a/b: Flow cytometry of human PBMCs (website).
CD40: Flow cytometry of human peripheral blood lymphocytes (website).
CD169: Flow cytometry of monocytes stimulated with IFNg and TNFa for three days (website).
CD117: Flow cytometry of human myeloid cell line TF-1 (website).
CD3: Flow cytometry of human PBMCs (website).
CD38: Flow cytometry of human PBMCs (website).
CD207: Flow cytometry of human monocyte-derived Langerhans cells (website).
CD206: Flow cytometry of human monocytes stimulated with GM-CSF for three days (website).
CD226: Flow cytometry of human peripheral blood lymphocytes (website).
HLADR: Flow cytometry of human PBMCs (website).
Axl: Flow cytometry of HeLa cell line (website).
CD209: Flow cytometry of human monocyte-derived dendritic cells (website).
CD11b: Flow cytometry of human PBMCs (website).

Human Immunohistochemistry
CD8a: IHC of FFPE human tonsil (website).
DC-LAMP: IHC of FFPE lung tumor (website).
CD20: IHC of FFPE human tonsil (website).

Mouse Immunohistochemistry
CD3e: IHC of FFPE tonsil tissue (website).
CD8a: IHC of FFPE mouse spleen (website).
Gzmb: IHC of FFPE mouse spleen (website).
NCR1: IHC of FFPE mouse spleen (website).

Mouse Immunofluorescence
FCER1A: Flow cytometry of MC/9 cell line (website).
CD117: Flow cytometry of mouse bone marrow (website).
Mac1: Flow cytometry of mouse splenocytes (website).
Gr1: Flow cytometry of mouse splenocytes (website).
B220: Flow cytometry of mouse splenocytes (website).
CD3: Flow cytometry of mouse splenocytes (website).
CD150: Flow cytometry of mouse bone marrow (website).
Sca-1: Flow cytometry of mouse bone marrow (website).
anti-armenian hamster IgG: ELISA (website).
anti rat Ig: ELISA (website).

In vivo
IL-4: Western blot (website).
FCER1A: Flow cytometry of MC/9 cell line (website).
CD200R3: Flow cytometry of mouse bone marrow in and ability to deplete basophils in vivo (Hajime Karasuyama lab).
PD-L1: Western blot (website).
Rat IgG1 isotype control: Western blot (website).
Armenian Hamster IgG isotype control: Western blot (website).
Rat IgG2b isotype control: Western blot (website).

Eukaryotic cell lines

Policy information about cell lines and Sex and Gender in Research

Cell line source(s)	KP cells were a gift from Tyler Jacks, who generated the line (Du Page et. al., 2009, Nature Protocols, PMID: 19561589). HKP1 cells were a gift from Vivek Mittal, who generated the line (Choi et. al., 2015, Cell Reports, PMID: 25704820). B16-F10 cells were obtained from the American Type Culture Collection.
Authentication	Cells were functionally validated via intravenous tail vein injection into mice and monitoring of tumor growth in lungs.
Mycoplasma contamination	All cell lines routinely tested negative for mycoplasma contamination.
Commonly misidentified lines (See ICLAC register)	No commonly misidentified cell lines were used.

Animals and other research organisms

Policy information about studies involving animals; ARRIVE guidelines recommended for reporting animal research, and Sex and Gender in Research

Laboratory animals	C57BL/6 mice were obtained from Charles River Laboratories (Wilmington, MA). Zbtb46-Cre (strain#:028538), CD4-Cre (strain# 022071) S100a8-Cre (strain #021614), Cx3cr1-Cre (strain# 025524), and CD45.1 (strain# 002014) were obtained from Jackson Laboratories (Bar Harbor, ME). CD169-Cre mice were a gift from Paul Frenette. IL4-eGFP (4get) mice fully backcrossed to the C57BL/6 background were obtained from Brian S. Kim. Il4rafloxed mice were generated by Cyagen (Santa Clara, CA). Briefly, CRISPR/Cas9 editing was used to generate mice with loxP sites flanking Exon 4 of the Il4ra gene, located on mouse Chromosome 7. Both male and

	female mice were used, and we observed no differences between sexes in any experiment. Littermate controls were used in all experiments. All experiments were initiated when mice were between 8-12 weeks of age. . Mice were housed in specific-pathogen free conditions at 21-22 degrees C at 39-50% humidity with a 12/12 hour dark/light cycle.
Wild animals	No wild animals were used.
Reporting on sex	Littermate mice of both sexes were used throughout this study. No sex-dependent effects were observed in any experiment. For the clinical trial presented in Figure 4, all participants were male as reported in Supplementary Table 5. Our clinical cohort of NSCLC patients used for plasma OLINK analysis consisted of 14 females and 15 males. All patient metadata, including sex, and OLINK values for patients can be found in Supplementary Table 3 and Supplementary Table 4, respectively.
Field-collected samples	No-field collected samples were used in this study.
Ethics oversight	All experiments were approved by, and in compliance with, the Institutional Animal Care and Use Committee of the Icahn School of Medicine at Mount Sinai.

Note that full information on the approval of the study protocol must also be provided in the manuscript.

Clinical data

Policy information about clinical studies

All manuscripts should comply with the ICMJE guidelines for publication of clinical research and a completed CONSORT checklist must be included with all submissions.

Clinical trial registration	NCT05013450
Study protocol	Protocol is available at ClinicalTrials.gov.
Data collection	Patients were recruited and samples collected at the Tisch Cancer Institute and the Blavatnik Family-Chelsea Medical Center at Mount Sinai over the period from 9/10/2021 to 9/6/2022
Outcomes	Primary Outcome The primary outcome for the Phase 1b portion of the study is dose limiting toxicity (DLTs) , based on the NCI Common Toxicity Criteria for Adverse Events (CTCAE), version 5.0. Secondary Outcomes The clinical secondary outcomes of this trial include Safety and Tolerability: Toxicity is assessed according to the NCI Common Toxicity Criteria for Adverse Events (CTCAE), version 5.0. Best overall response (BORR) is a combined percent of the patients experiencing a partial response (PR) or a complete response (CR) at any point within the first year from the initiation of therapy, or until the documented progression of disease or start of a new anti-cancer therapy. Progression-free survival (PFS) is defined as the time in days from the first administration of dupilumab until documented progression of disease on imaging or death. Overall survival (OS) is defined as the time in days from the first administration of dupilumab until documented death from any cause. Duration of response (DOR) is defined as the time from which a patient achieves either a PR or a CR until subsequent progression of disease is documented radiographically or clinically. Exploratory Outcomes Exploratory Scientific Outcomes The primary non-clinical outcome of this trial is the creation of dynamic atlases documenting the evolution of a patient's TME, comparing pre-treatment biopsy and blood with subsequent biopsy and blood collection. The formation of this atlas involves histologic, immunologic, genetic and radiomic characterization of the tumor across time.

Flow Cytometry

Plots

Confirm that:

☒ The axis labels state the marker and fluorochrome used (e.g. CD4-FITC).

☒ The axis scales are clearly visible. Include numbers along axes only for bottom left plot of group (a 'group' is an analysis of identical markers).

☒ All plots are contour plots with outliers or pseudocolor plots.

☒ A numerical value for number of cells or percentage (with statistics) is provided.

Methodology

Sample preparation	Mouse lung, blood, and bone marrow were prepared as single cell suspensions (see methods). Red blood cells were lysed using ACK Lysis Buffer.
Instrument	BD LSRFortessa
Software	FACSDiva v8.0.2 software.
Cell population abundance	Purity and abundance were evaluated by flow cytometry
Gating strategy	Gating strategies for all populations can be found in Supplementary Information. Below we describe this strategy for all populations in written form. For all populations, cells were first gated on intact events based on FSC-A vs SSCA, then gated on singlets based on FSC-A vs FSC-H, then gated on live cells based on FSC-A vs Viability Dye/DAPI (further analyzing Viability Dye/DAPI-negative cells). Note, Lineage = Ly6g, CD3e, B220, NK1.1, CD11b, Ter-119. HSC-LT and HSC-ST: 1. Gate on FSC-A vs Lineage was set to exclude lineage+ cells. 2. Gate on Sca-1 vs c-KIT was set to enrich double-positive cells. 3. Gate on CD135 vs CD150 was set to exclude all CD135+ cells. 3. Gate on CD48 vs CD150 to exclude all CD48+ cells. HSC-LT are CD150+ and HSC-ST are CD150-. CMP and MDP: 1. Gate on FSC-A vs Lineage was set to exclude lineage+ cells. Gate on Sca-1 vs c-KIT was set to enrich c-KIT+ Sca-1- cells. 3. Gate on CD16/32 vs CD34 was set to exclude CD16/32+ cells. 4. Gate on CD135 vs CD34 was set to exclude CD135+ cells. 5. Gate on Ly6c vs CD115 to exclude Ly6c+ cells. CMP are CD115-. MDP are CD115+. Bulk GMP, Ly6cNEG GMP, GP, cMoP: 1. Gate on FSC-A vs Lineage was set to exclude lineage+ cells. Gate on Sca-1 vs c-KIT was set to enrich c-KIT+ Sca-1- cells. 3. Gate on CD16/32 vs CD34 was set to enrich CD16/32+ CD34+ cells. 4. Gate on CD34 vs CD135 was set to exclude CD135+ cells. This population constituted bulk GMPs. 5. Gate on bulk GMPs Ly6c vs CD115. Ly6cNeg GMPs are double negative. GPs are Ly6c+CD115-. cMoPs are Ly6c+CD115+. Eosinophils: 1. Gate on SSC-A vs CD45 to enrich CD45+ cells. 2. Gate on CD11c vs CD45 to exclude CD11c+ cells. 3. Gate on CD11b vs Siglec F. Double positive cells are eosinophils. Basophils and ILC2: 1. Gate on CD3e, Ter-119, NK1.1, Ly6g, B220 vs c-KIT to enrich for double-negative cells. 2. Gate on FCER1A vs CD49b. Double positive cells are basophils. Continue gating within the double negative cells. 3. Gate on CD11b vs c-KIT to enrich double negative cells. 4. Gate on ST2 vs CD90.2. Double positive cells are ILC2. B cells, CD4 T cells, CD8 T cells: 1. Gate on SSCA-vs CD45 to enrich CD45-HI SSC-A-LO cells. 2. Gate on CD19 vs TCRb. CD19 single-positive cells are B cells. Continue gating on TCRb single positive. 3. Gate on CD4 vs CD8. CD8 single positive are CD8 T cells. CD4 single positive are CD4 T cells. NK cells: 1. Gate on SSCA-vs CD45 to enrich CD45-HI SSC-A-LO cells. 2. Gate on CD3e vs NK1.1. NK1.1 single positive cells are NK cells. Lung myeloid cells: 1. Gate on SSC-A vs CD45 to enrich CD45+ cells. 2. Gate on Ly6g vs CD11b. Double-positive cells are neutrophils. Continue on non-neutrophils. 3. Gate on CD64 vs MerTK. Double positive cells are macrophages. Within macrophages, CD11b+ cells are mo-macs and CD2+ cells are RTMs. Continue gating on non-macrophages. 4. Gate on MHC-II vs CD11c. Double positive cells are DCs. Within DCs, CD103+ cells are DC1 and CD11b+ cells are DC2. Continue gating on non-DCs. 5. Gate on CD11b vs Cx3cr1. Double positive cells are monocytes. Use Ly6c expression to discriminate Ly6c HI inflammatory monocytes from Ly6c LO patrolling monocytes. Blood myeloid cells: 1. Gate on SSC-A vs CD45 to enrich CD45+ cells. 2. Gate on FSC-A vs CD3e, CD19, NK1.1 to exclude CD3, CD19, and NK1.1+ cells. 3. Gate on CD11b vs Ly6g. Double positive cells are neutrophils. Continue gating on non-neutrophils. 3. Gate on CD11b vs CD115. Double positive cells are monocytes. Monocytes can be further separated by Ly6c staining into Ly6c HI inflammatory and Ly6c LO patrolling monocytes. Human blood CyTOF. (Pre-gating on live CD45+ cells, obtained from debarcoding). 1. Gate on CD19 vs CLEC9A. CD19 positive cells are B cells. Among B cells, CD38+CD27+ cells are plasma cells. Continue gating on non-B cells. 2. Gate on CD3 vs CD56 to enrich CD3+ T cells. Among T cells, CD8+CD45RA+CD27+ cells are effector CD8 cells. Continue gating on CD3-CD56- cells. 3. Gate on CD66b vs CD11b. Double positive cells are granulocytes. Continue gating on non granulocytes. Gate on CD14 vs CD16. CD14+ cells are inflammatory monocytes. CD16+ cells are patrolling monocytes. Together, these two populations constitute the monocyte fraction.

☒ Tick this box to confirm that a figure exemplifying the gating strategy is provided in the Supplementary Information.